Journal of Ultrafine Grained and Nanostructured Materials
https://jufgnsm.ut.ac.ir
Vol. 59, No.1, June 2026, pp. 65-89
Print ISSN: 2423-6845 Online ISSN: 2423-6837
DOI: 10.22059/jufgnsm.2026.01.06

# Hot Corrosion Resistance of Severely Plastically Deformed Alloys: A Review

***Mohammad Emami[1]*, Reza Taghiabadi[2]****

*[1] Department of Materials Science and Engineering, University of Bonab, Bonab, Iran*
*[2] Department of Metallurgy and Materials Science, Imam Khomeini International University (IKIU), Qazvin, Iran*

*Recieved: 4 April 2026; Accepted: 25 April 2026*

**Corresponding author, E-mail:* memami@ubonab.ac.ir , taghiabadi@ikiu.ac.ir

**ABSTRACT**

Hot corrosion (HC) causes failure in high temperature components, such as gas turbines, power plants, refineries, fluidized bed combustion systems, pipelines, and industrial waste incinerators. The HC resistance of the alloys relies on the formation of resistant oxide scales. In this review paper, different atmospheres and salt compositions causing HC, the pertinent mechanisms, and the influencing factors such as time, temperature, and alloy's composition were briefly discussed. Despite extensive research on the effect of alloy's composition on the HC behavior, the alloy's microstructure/defect structure which can affect the kinetics of diffusional processes during HC has been less noticed. Based on the survey on several articles on the effects of various SPD techniques on the microstructure/defect structure of the alloys, it was noted that the severe plastic deformation (SPD), featuring highly distorted crystal lattices, and a high density of lattice defects such as vacancies, dislocations, twins, and stacking faults together with considerable grain refinement through the formation of high angle grain boundaries is a potential technique to enhance the HC resistance of the alloys through the enhanced rate of the formation of protective oxide scales, and their healing up after a possible corrosion attack. Therefore, a number of few studies on the HC behavior of the SPDed materials were reviewed in the last section of this paper and the positive effect of the SPD on the HC resistance of the alloys was confirmed.

***Keywords:*** *Hot corrosion, Sever plastic deformation (SPD), Surface severe plastic deformation (SSPD), Ultrafine grained.*

## 1. Introduction

Equipment used at high temperature environments like combustion systems and hot sections of the aerospace gas turbines suffer from a kind of severe degradation called "hot corrosion", because of the formation of corrosive deposits on their hardware [1]. The corrosive deposits result from the incorporation of environmental media such as seawater, $Na_2O$, $K_2O$, NaCl, $NaVO_3$, $Na_2SO_4$, and other corrosive materials into the service atmosphere [2-4]. HC of the components can reduce their service life, lower their efficiency and make catastrophic damage to the equipment such as gas turbine engines [5] and blades of energy production turbines [6].

In the outer surface of the boiler tubes, another kind of HC damage may occur due to the liquid deposit formation called "fire-side corrosion". In coal fired boilers, the liquid phase is a mixture of $Na_3Fe(SO_4)_3$ and $K_3Fe(SO_4)_3$ having a melting point of about 555 °C whilst in oil fired boiler it is a mixture of $V_2O_5$ with either $Na_2O$ or $Na_2SO_4$ with a melting point of below 540 °C [7]. Molten salt corrosion is the other type of HC occurring for

example in concentrated solar power (CSP) plants utilizing solar-salt, comprising a mixture of fused 60 wt. % $NaNO_3$-40 wt. % $KNO_3$, as thermal energy storage (TES) media and heat transfer fluid (HTF). For higher operating temperatures, a ternary $MgCl_2$–KCl–NaCl mixture has been proposed [8]. This corrosion type has been known as one of the main issues which demands more resistant alloys and coatings [9]. Understanding materials corrosion in the presence of molten salt mixtures used as TES media and HTFs is indispensable for CSP development [8]. However, the corrosion mechanisms in such conditions (i.e. under a thick molten salt rather than a thin film of fused salt) are quite different from the deposit-induced HC damage in turbine blades.

Because multiple failure mechanisms such as HC, fatigue and creep are involved in gas and energy turbine systems, up to now various Fe-, Ni-, Co-, and Ti-based high temperature alloys and anti-corrosion coatings such as Ni-Cr, aluminide, MCrAlY(X), silicide coatings have been considered as the solution. However, various research works have indicated that these coating are susceptible to cracking and/or flaking under the influence of gas impact. Surface strengthening methods such as SPD processing have been also considered as another effective solution. It is believed that the SPD-related microstructural changes can influence HC behavior of the alloys by affecting the diffusional processes so that their surface can rapidly form a dense and protective oxide layer at the initial HS stages.

However, apart from the scalability issues associated with some SPD techniques, the SPDed alloys may encounter other challenges at the high temperature applications namely microstructural instability, possible recrystallization, long term degradation, and loss of creep resistance. Therefore, the implementation of SPD processes to improve the HC resistance of engineering alloys faces serious limitations. The literature review also reveals that limited attention has been reported so far on HC of fine-grained SPDed microstructures most of which focus on the influence of SPD on the HC of alloys at relatively low temperatures (below 750 °C) corresponding to low temperature HC (type II). This review paper attempts to provide a genuine bridge between the SPD-induced microstructural evolutions and HC of alloys, but before that, it briefly introduces the HC and related mechanisms and the SPD processes with an emphasis on the microstructural features formed during the SPD.

## 2. Origin of hot corrosion

A variety of molten salts including CaO–MgO–$Al_2O_3$–$SiO_2$ (CMAS) stemming from atmospheric dust or volcanic eruptions with a melting temperature of about 1200 °C [10-12], $Na_2SO_4$–$V_2O_5$ salts, and alkali metal chlorides from low quality fuel combustion [4] can cause HC. When the combustion gas contains high amounts of sulfur or when the equipment is used in marine atmosphere where the chlorine salts are involved in the air, the high temperature components can be covered with a mixture of salts such as NaCl, KCl, and $Na_2SO_4$ (salt deposit) under which HC reactions occur [13].

The humid air containing floating NaCl microparticles can also cause severe HC of the Ni-based superalloys at elevated service temperatures. When the air is sucked into the turbine engine, the NaCl particles with a larger specific density than air easily deposit on the components [5]. Sulfur with Na or K in very minute amounts can create enough $Na_2SO_4$ or $K_2SO_4$ to start the corrosion attack. Up to 2600 ppm of $Na_2SO_4$ and 19000 ppm of NaCl from saltwater may be present in unfiltered air, which worsens the corrosive effects of the environment on the components of shipboard marine gas turbines [14]. The salt deposition can happen through either chemical or physical deposition. In the chemical deposition, the vapor pressure of a compound such as $Na_2SO_4$ in the vapor phase exceeds its equilibrium partial pressure for the substrate temperature. In physical deposition, some solid or liquid salt can detach from an upstream component and attach to a hot substrate upon impact [15].

The incorporation of other species can significantly alter the thermophysical properties and the subsequent corrosiveness of the fused deposit. For instance, the melting point of $Na_2SO_4$ is 884 °C which can be reduced to about 620 °C by the addition of NaCl due to a eutectic mixture formation. Also, in combustion gases, NaCl may react with sulfur dioxide and oxygen, forming $Na_2SO_4$ through the following reaction [16]:

$$2NaCl + SO_2 + O_2 \rightarrow Na_2SO_4 + Cl_2 \quad (1)$$

KCl and $K_2SO_4$ also form a eutectic mixture with a melting point of 690 °C, which is below the melting temperature of each salt [17]. When V impurity is present in the fuel, highly corrosive liquid phases of V have been reportedly formed at temperatures as low as 535 °C, depending on the ratio between Na and V [16].

## 3. The principles of hot corrosion

### 3.1. Hot corrosion mechanism

Different bulk and coating materials have been evaluated under a variety of salt deposits in the literature. For example, a mixture of 60 wt.% $Na_2SO_4$ + 40 wt.% $MgSO_4$ was used by de Castilho et al. [18] to evaluate the HC properties of a NiCoCrAlY coating. Wang et al. [13] employed

two types of salt mixtures, 50% NaCl-50% KCl and 43% NaCl-43% KCl-14% $Na_2SO_4$ to evaluate the HC behavior of Ni16Cr13Co4Mo superalloy. Based on the material, corroding salt, and test conditions different mechanisms have been proposed for the deposit-induced HC. Molten salts can destroy protective metal oxide films and also directly react with the alloy to generate some low-melting eutectic salts, and deplete the substrate from protective alloying elements like Cr and Al. Also, the reactions that cause alloy damage can be accelerated at elevated temperature environments, causing a more rapid degradation of the alloy [4].

During the initiation/incubation stage of the HC, protective oxide scales form on the alloy [19]. However, when the alloy is exposed to a corrosive atmosphere for longer times, aggressive species such as oxygen, sulfur, and chloride ions can diffuse to the alloys substrate and degrade the material [13, 19].

According to the literature, HC is classified in type I and type II HC. The former, typically referred to high temperature HC (HTHC), occurs at higher temperatures (800-950 °C) and the latter being typically more severe, is associated with exposures at lower temperatures (600-750 °C) which is known as low temperature HC (LTHC) [20-23]. Generally, Type-I HC is accompanied by internal sulfidation, dissolution of protective chromia/alumina layers, and severe base material loss [24]. The salt composition can profoundly affect the corrosion mechanism and the damage degree.

It has been reported that molten $Na_2SO_4$ directly interacts with alloying elements, resulting in the formation of related oxides and sulfides. During this time, the produced sulfur will react with alloying elements like Ni, Cr, and Fe within the matrix, resulting in low-melting-point sulfides like $Ni_3S_4$ with a melting point of 356 °C ($xM + yS = M_xS_y$). These sulfides subsequently create low-melting-point eutectic salts with mixed salts, resulting in a molten salt environment. Nonetheless, because of the high oxygen partial pressure at the interface, the generated sulfides cannot remain stable for an extended period and are then oxidized to produce the relevant metal oxides ($M_xSy + y/2\ O_2(g) = M_xO_y + yS$). The emitted sulfur quickly penetrates deeper into the alloy's interior via defects in the corrosion layer (like cracks, pores, etc.), resulting in internal sulfidation of the matrix. Additionally, $Na_2O$, being an alkaline oxide, can destroy the protective oxide layer on the alloy surface via the reaction $A_2O_3 + Na_2O = 2NaAO_2$ [4].

As the oxide film integrity is lost, components like sulfur and oxygen, along with corrosive media, will persistently penetrate through the defects, resulting in the formation of sulfides and oxides within the matrix [4]. Before the final failure, the material is damaged in several steps. First, the growth and localized breakdown of the oxide scale causes slight roughening of the surface, without any Cr depletion in the substrate or loss of mechanical properties. Then, oxide layer breakdown continues and Cr depletion starts. Later, the oxidation attack penetrates more deeply into the base material, scale thickening and removal as large blisters happens [16]. Ellingham-Richardson diagram of alloying elements reacting with molten $Na_2SO_4$ can be seen in Fig. 1.

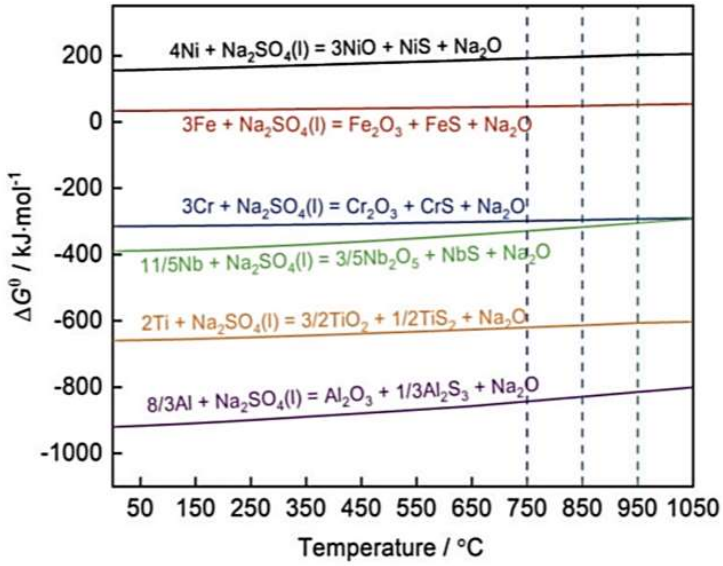


Fig. 1- Ellingham-Richardson diagram of alloying elements reacting with molten $Na_2SO_4$ [4].

The oxide dissolution in the salt can occur in either a basic or acidic dissolution mechanism. In the case of fused $Na_2SO_4$, the oxide solubilities in this salt for 1 atm and T = 927 °C are summarized in Fig. 2 [25]. Considering NiO, basic dissolution happens through the following reaction:

$$2NiO + \frac{1}{2}O_2 + O^{2-} \rightarrow 2NiO_2^{2-} \quad (2)$$

and acidic dissolution occurs via the following reaction:

$$NiO \rightarrow Ni^{2+} + O^{2-} \quad (3)$$

In general, HC of superalloys with high contents of Al and Cr is often reported to occur according to the basic fluxing mechanism. Conversely, HC of alloys with high contents of W, Mo and V is often reported to follow the acidic fluxing mechanism [16].

Type-II HC, as a new corrosion mechanism, was found around 1975. It includes pitting, irregular alloy-oxide interface, and lacks sub-scale sulfides. In Type-II HC, $Na_2SO_4$ creates eutectic mixtures with metallic inorganic compounds like $Na_2SO_4$–$CoSO_4$ or $Na_2SO_4$–$NiSO_4$, reducing the overall melting temperature and starting the corrosion process. These inorganic metal compounds stem from $SO_3$ in the combustion gas and the metal, making Type-II HC dependent not only on temperature but also on the partial pressure of $SO_3$ gas [4, 16]. Type-II HC is marked by pitting and localized attack. The initiation of pitting is presently being examined and has been associated with various factors such as grain boundaries, precipitates, gas atmosphere, and the presence of salt deposits. In the case of Co-based superalloys, the pit formation results from mixtures of $Na_2SO_4$ and $CoSO_4$ with low melting temperatures as low as 540°C. $CoSO_4$ itself is a corrosion product of a reaction between the surfaces of Co-based blades and $SO_3$ from the combustion gas [16].

### 3.2. Factors affecting the hot corrosion behavior

A number of factors including the temperature, corrosive atmosphere, exposure time, and alloy's composition affect the alloys behavior in HC conditions [26-28]. In high temperature corrosion studies, the alloy is typically corroded more severely at higher temperatures and longer exposures. However, as observed in section 3-1, because of the complex environments, these behaviors can be more complicated. Regarding alloy's composition, W, V and Mo which are exceptionally beneficial for the mechanical properties, can make the alloy highly susceptible to HC [29]. Alloying elements like Ce, La, Zr, Y, and Sc are reported to enhance the adhesion between the alloy and the oxide scale and improve the corrosion resistance of the alloy [30]. According to the literature, Al, Ti, and Nb are also beneficial in HC conditions [31]. In the study of Gregoire et al. [32], Cr was found to increase type II HC resistance by forming mixed $(Cr,Al)_2O_3$ scales.

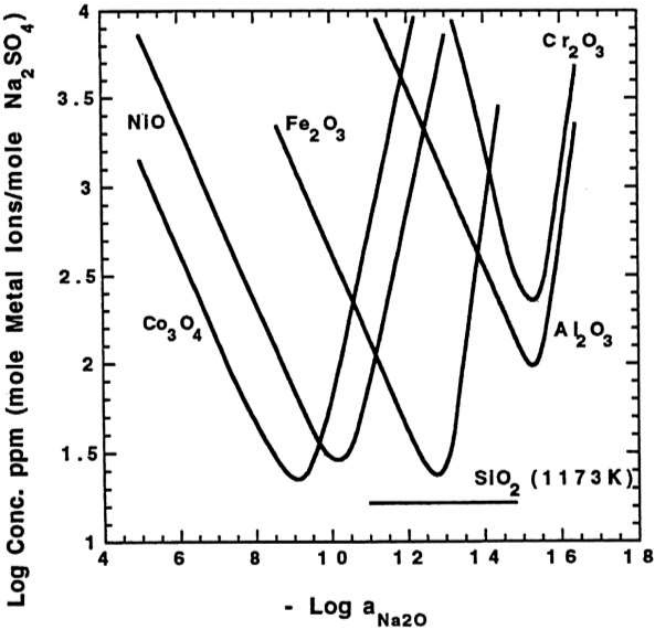


Fig. 2- Measured oxide solubilities in molten $Na_2SO_4$ at 927 °C and oxygen pressure of 1 atm [25].

Besides the alloy composition which in turn can influence the type and quality of the protective oxide scale formed on the surface, the corrosive salt has a crucial role in the HC behavior of alloys. For instance, it is widely believed that a molten chloride salt can easily dissolve a $Cr_2O_3$ oxide scale and attack the underlying substrate [33]. Furthermore, in chlorine containing atmospheres, volatile chloride compounds such as $CrCl_3$ may form and promote metal chlorination and volatilization on the surface, ending in blistering and disrupting the integrity of the protective oxide layer [34, 35]. Under mixed salts deposits, the HC behavior can be more complicated. The HC behavior of a Ni-base single crystal at 900 °C, investigated under three different mixed salts, showed that a salt mixture of $Na_2SO_4$+NaCl+$NaVO_3$ was the most aggressive, followed by $Na_2SO_4$ + $NaVO_3$, and $Na_2SO_4$ + NaCl [6]. In a study on the HC behavior of Ni16Cr13Co4Mo alloy in molten NaCl-KCl and NaCl-KCl-$Na_2SO_4$, the HC was accelerated at higher temperatures and in the $Na_2SO_4$ containing salt, forming a defective outer chromia layer and an inner $TiO_2$-$Al_2O_3$ layer, while in the NaCl-KCl salt a corrosion layer of $Cr_2O_3$ was formed [13]. In the HC study of Ni based superalloys in multiple salts, it was figured out that the HC attack in $Na_2SO_4$+NaCl salt was more severe than in $Na_2SO_4$ +$K_2SO_4$ salt. It was attributed to the cracking and spalling of $Cr_2O_3$ oxide scale by the NaCl addition. $V_2O_5$ also can make the alloy more susceptible to HC due to increasing the salt acidity [6].

Besides the above-mentioned factors, the microstructure can affect the HC resistance of the alloy. Secondary phases might lead to an accelerated attack, either along phase boundaries or by selective attack of one phase. It has been suggested to avoid coarse refractory metal carbides [29]. Wei et al. [19] suggested that the HC resistance of a single crystal Ni-based superalloy was a function of alloy orientation. It was attributed to the varying diffusivities for active cations in different orientations. Bhuyan et al. [36] have reported the significant effects of the grain boundary characteristics on the HC resistance of superalloys. grain boundary area fraction and crystal orientation of IN718 which depends on the build direction, was reported to determine the alloy's oxidation resistance [37]. Despite many research works carried on the effects of chemical compositions of the alloys and salts on the HC behavior of the materials, the effects of the alloy's microstructure on it is limited.

## 4. Overview of SPD processes

SPD is a prospective way for microstructural refinement and enhancement of the properties of engineering materials [38-40]. High strength combined with high ductility, low temperature superplasticity, enhanced creep resistance, improved hydrogen storage capability, photocatalytic hydrogen production/$CO_2$ conversion, enhanced superconductivity, improved thermoelectric performance, higher radiation resistance, and improved corrosion resistance and biocompatibility are some of the merits of SPD processed materials [41, 42]. Before reviewing the latest researches conducted on the HC behavior of engineering alloys, a deeper understanding of the SPD processes emphasizing on their microstructural changes, possibly affecting HC behavior is sought.

### 4.1. Principles of SPD processes

It is believed that the interrelationship between the processing, composition, structure, and properties of a material is the essence of materials science and engineering. In conventional metal-forming processes, the microstructure and properties of the material are mainly controlled by thermally activated processes such as phase transformation which are on thermodynamics basis and in some cases with the aid of mechanical processes [43]. Imparting large plastic strains to a workpiece by conventional metal forming techniques is challenging because of the dimensional changes, internal defects, and crack formation. Highly expensive tools should be designed to endure repeated high stresses during material forming and high hydrostatic stresses [44].

What makes SPD distinct from conventional forming processes is the large strains imposed on the workpiece without any significant changes in the overall dimensions. This is attained by special tool geometries that prevent the material from free flow and thereby produce significant hydrostatic compressive stresses. The presence of this hydrostatic pressure is a clue to obtain the high strains required for the significant grain refinement [44, 45].

As shown in Fig. 3, the SPD process can simply be analogous with a hammer impacting and crushing a pane of glass. The glass can be associated with the microstructure of the material, and the enveloping frame can be related to the role of hydrostatic pressure in the SPD process. The hammer impact resembles the high strain placed on the material by the SPD process, and the crushed glass visualizes the transformation from the coarse grain to the UFG/NS materials [44].

In the SPD processing, obtaining crack-free uniform UFG/NG structures with dominant HAGBs, spread through the volume, for a uniform and considerable change in material properties is required. The grain interiors usually possess a substructure with high dislocation density due

to highly distorted crystal lattices. These are not attainable in conventional plastic deformation methods such as drawing, rolling, and extrusion in which the microstructures developed are otherwise LAGBs [43].

### 4.2. Severe plastic deformation processes

The SPD processes can be categorized into three bulk-SPD, surface-SPD and powder-SPD methods. In bulk-SPD, the goal is to refine the entire microstructure of a reasonably large-size material, knowing that the surface is inevitably affected. In surface-SPD, only surface and sub-surface layers are modified, while the sample interior remains mostly unchanged. In powder-SPD, the material is in the powder form, and the strain is placed on both the surface and core of the powder particles usually by utilizing ball milling methods [43, 46].

Some SPD processes developed for deforming bulk metals include, HPT, incremental high-pressure torsion (IHPT), single-task incremental high-pressure torsion (SIHPT), high-pressure torsion extrusion (HPTE), ECAP, rotary-die ECAP, side-extrusion, multi pass ECAP, torsional-equal channel angular pressing (T-ECAP), expansion ECAP (Exp-ECAP), ECAP with parallel channels, incremental ECAP (IECAP), dual equal channel lateral extrusion (DECLE), channel angular pressing with converging billets, torsion extrusion (TE), multiple direct extrusion (MDE), accumulated extrusion (AE), pure shear extrusion (PSE), equal channel forward extrusion (ECFE), C-shape equal channel reciprocating extrusion (CECRE), twist extrusion (TE), elliptical cross-section spiral equal channel extrusion (ECSEE), planar twist extrusion (PTE), axisymmetric forward spiral extrusion (AFSE), multidirectional forging (MDF), cyclic closed-die forging (CCDF), multiaxial incremental forging and shearing (MAIFS), repetitive forging (RF), repetitive upsetting (RU), cylinder covered compression (CCC), repetitive upsetting and extrusion (RUE), cyclic extrusion compression (CEC), cyclic expansion extrusion (CEE), accumulative roll bonding (ARB), accumulative back extrusion (ABE), cyclic forward backward extrusion (CFBE), half-channel angular extrusion (HCAE), accumulative channel-die compression bonding (ACCB), machining, twist channel angular pressing (TCAP), twist channel multi angular pressing (TCMAP), and cyclic extrusion compression angular pressing (CECAP) [43, 46,47-50].

Some SSPD processes include sand blasting, air blast shot peening (ABSP), surface mechanical rolling treatment (SMRT), occasionally called surface mechanical grinding treatment (SMGT), laser shock peening (LSP), fast multiple rotation rolling (FMRR), ball burnishing (BB), flap peening, micro-shot peening, acoustic/hydrodynamic cavitation peening, and friction-based methods (friction stirring, friction hardening), and ultrasonic-based processes such as ultrasonic shot peening (USSP/USP) processes, ultrasonic impact treatment (UIP), ultrasonic nanocrystalline surface alteration (UNSM), ultrasonic cold forging method (UCFM), rotating pins ultrasonic peening (RPUP), ultrasonic surface rolling (USR) techniques, ultrasonic surface rolling treatment (USRT), ultrasonic surface rolling process (USRP), and surface ultrasonic rolling treatment (SURT), ultrasonic deep cold rolling (UDCR), ultrasonic abrasion finishing (USAF), and ultrasonic vibration-supported ball burnishing (UVABB) [51,52].

### 4.3. Microstructural features of SPDed metals and alloys

In SPD techniques, a piece of material is largely strained usually under high pressures. This commonly makes significant microstructural changes including grain refinement to the submicrometer/ nanometer levels. It is established that the grain size reaches a constant level at large strain [53].

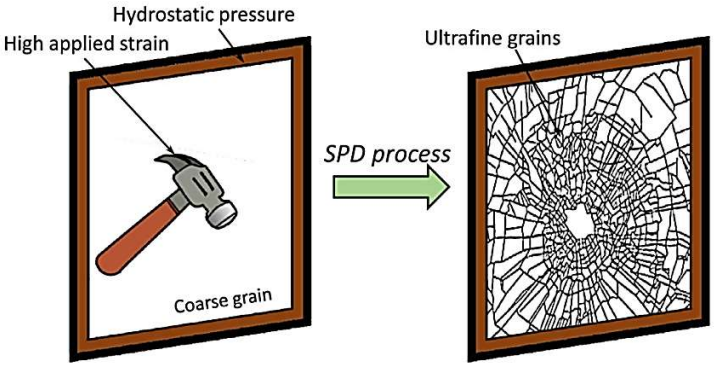


Fig. 3- Simulation of the SPD process with hammer impact on glass [44].

The microstructural changes in the SPD are not limited to the formation of UFG structures. It may also be used to engineer GB structures and generate various kinds of defects such as twins, dislocations, stacking faults and vacancies as well as some unique microstructural features including grain boundary segregation, and precipitate formation/dissolution, texture development, formation of nanoparticles, nano clusters, and etc. [53, 54]. SPD processing may also lead to unusual phase transformations such as dissolution of second phases, precipitation, amorphization, allotropic phase transformations, and the unusual combinations of SPD-induced diffusive and displacive (martensitic) phase transformations [54]. In the following, some of the most important SPD-induced microstructural changes that appear to affect the HC behavior of metals and alloys are reviewed.

**4.3.1. Formation of ultrafine grains**

In SPD processing, large numbers of dislocations arrange themselves in low-energy configurations to form LAGBs and when the sample is further strained, they evolve into reasonably homogeneous arrays of UFGs separated by boundaries having high angles of misorientation. In addition, very few lattice dislocations are observed in the smaller grains, whereas high densities of lattice dislocations are in the grains of intermediate sizes and subgrains are present in the larger grains [55].

In conventional metallurgy, grain refinement primarily occurs through the recrystallization taking place during the annealing heat treatment after plastic deformation. However, in the as-SPDed materials, UFG structures are observed without annealing treatment. Figs. 4a and 4b show TEM micrographs of ARB-processed IF steel and 99% pure Al, respectively showing ultrafine lamellar structures with an average lamellar spacing of about 200 nm. A mechanism for grain subdivision is schematically illustrated in Fig. 4c [53].

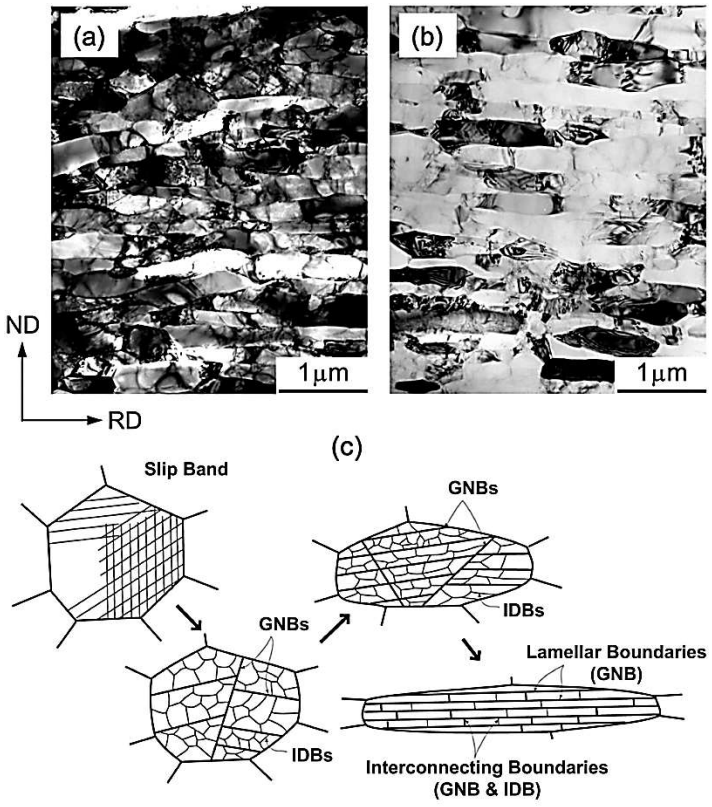


Fig. 4- (a, b) Typical ultrafine-grained microstructures obtained by ARB, (a) IF steel, (b) 99% pure Al, (c) Schematic illustration of the grain subdivision mechanism [53].

In polycrystalline materials, multiple slip systems including the primary slip system with the highest resolved shear stress are activated in a grain owing to the constraints by the neighboring grains. The activation of multiple slip systems in different grain areas causes various local crystal rotations. This leads to the evolution of misorientation between the neighboring areas in a process known as "grain subdivision", resulting in geometrically necessary boundaries (GNBs) [53]. The GNBs usually are largely misoriented after relatively large plastic strain. The domains divided by GNBs are highly dislocated regions, tending to form low-energy configurations that are called incidental dislocation boundaries (IDBs) [48]. During the SPD, the original grains are subdivided by GNBs and IDBs until final nanometer-size grains form by increasing plastic deformation [53].

Sufficient dislocations and high local stress can drive the nucleation and growth of deformation nanotwins in SPD processes [57]. In nanocrystalline metals, twinning is facilitated with decreasing grain size to a certain level, reaching a maximum twinning probability, after which twinning becomes more difficult. Several factors including a relatively low SFE, a low deformation temperature, and a high strain rate can affect the formation of nanotwins. Fig. 5 shows an HRTEM image of a UFG Cu, illustrating 10–20 nm twins, after ECAP and cold rolling at the liquid nitrogen temperature. Deformation twinning can lead to an enhanced strength and ductility in nanocrystalline materials [54].

### 4.3.2. Grain boundaries

UFG and NG materials contain a very high density of GBs, which is responsible for the occurrence of advanced properties. The structure and strain state of GBs can significantly affect the stability, mechanical performance, and the grain-boundary diffusion. The UFG metals are often referred to as "interface-controlled materials" [43, 58]. Depending on the SPD processing route, different types of GBs including low-/high-angle boundaries, special and random, equilibrium/non-equilibrium boundaries with strain-distorted structures and extrinsic dislocations are formed [54].

The non-equilibrium state of HAGBs and the related phenomena (diffusion, segregation, etc.) play significant roles in unusual properties of the UFG materials. The non-equilibrium grain boundary state formation is characterized by three main features, namely enhanced free volume, the presence of long-range elastic stresses (Fig. 6), and excess grain boundary energy. The free volumes with an average size of one to two vacancies are considered to represent structural elements of the metastable and highly disordered interfaces of nanocrystalline metals, which are unlikely to exist, e.g., in symmetric tilt or twist boundaries of conventional polycrystalline metals. However, the term has been utilized and accepted by the working community in SPD, where it is used to describe GBs with strain-distorted structures [43, 58].

The following phenomena/processes contribute to the non-equilibrium GBs in SPD-processed materials [43, 58]:

-Redistribution of the related excess free volume, the release of local strains/stresses

-Abundant vacancies and vacancy-like defects in interfaces produced by severe deformation

-Segregation can be especially important in alloys; chemical effects may be important in alloys and compounds affecting the atomic redistribution and retardation, e.g., the stress/strain relaxation

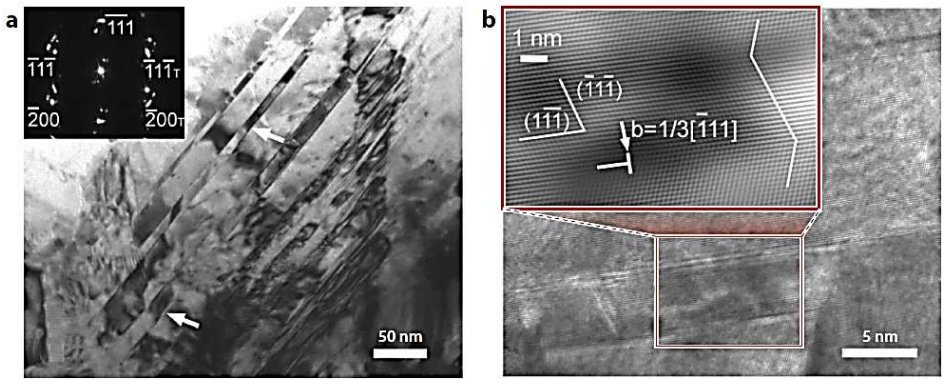


Fig. 5- TEM images of a typical grain with a high density of deformation twins in a UFG Cu processed by ECAP with subsequent cold rolling. (a) The white arrows indicate the positions of the twins; the diffraction pattern of this region is seen in the inset. (b) Inset is an HRTEM image of this region with its atomic-crystalline structure indicated [54].

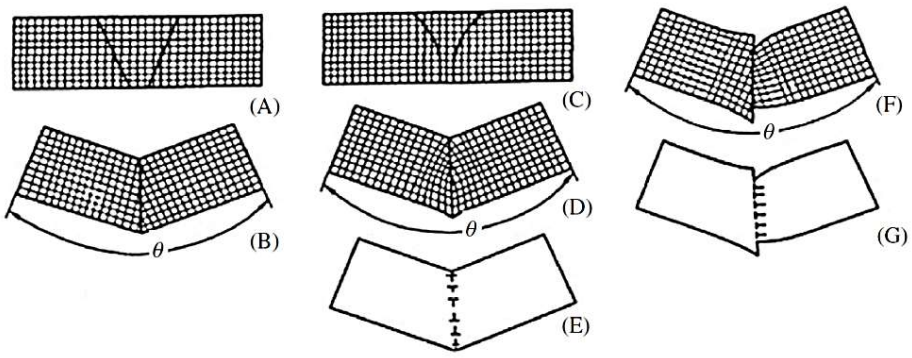


Fig. 6- Formation of a grain boundary via imaginary cuts: (A)→(B) obtaining an equilibrium grain boundary without mesoscopic strain, (C)→(D) and (A)→(F) obtaining non-equilibrium with deformation that is required for crystal joint—bending and tension—compression, respectively, GBs. Networks of fine lines do not show a crystal lattice but are given only to show elastic fields; (E) and (G) schemes of complexes of grain boundary dislocations (GBD) creating the same character of elastic fields as in (D) and (F) [43].

Generally, concerning the grain boundary structure in SPD-processed UFG materials, recent studies conclude that the width of non-equilibrium GBs is in the order of a few nanometers, which is substantially larger than the width of relaxed HAGBs at the annealed CG materials. Moreover, strain-distorted structure non-equilibrium GBs, as seen in UFG materials, exhibit an increased width, increased free-energy density, correspondingly large residual microstrain, and high density of dislocations associated with the near-boundary region [43, 58].

**4.3.3. Grain boundary segregation**

The interaction between solutes (or impurities) and grain boundaries might significantly affect UFG structures resulting from SPD processing. It both affects the dynamic recovery mechanisms during SPD processing and the resulting steady-state grain size and leads to grain boundary segregations. Such grain boundary segregations have been observed in commercial Al alloys, steels, and Ti [53]. All lattice defects created during SPD processing may influence the atomic mobility and promote grain boundary segregations; dislocations can drag solutes or act as diffusion pipes. Grain boundaries are also fast diffusion paths and can drag solutes when they move during the deformation, and strain-induced vacancies can directly enhance the atomic diffusion. Strain-induced grain boundary segregations may also promote phase separation in super-saturated solid solutions under SPD conditions, such as dynamic precipitation in the Al-Zn or Al-Cu systems. Indeed, since grain boundaries are fast diffusion paths, these segregations provide a strong flux of solutes toward particles that nucleate at triple lines [54].

**4.3.4. Texture evolution**

Texture evolution is one of the prominent features of SPD processing. Texture is defined as the orientation distribution of crystallites in polycrystalline materials. It plays a major role in the grain refinement process during the SPD process. It also changes the strength, work hardening, plastic anisotropy, formability, corrosion behavior, grain refinement, and fracture properties of severely deformed materials [43, 53, 58].

Texture alters by the grain rotation. During deformation, small regions within a grain start rotating by the activation of different slip systems, leading to the formation of substructures [53]. Depending on the SPD process, the texture evolved can be either shear-based (such as ECAP, HPT, and FSP) or plane strain-based (such as ARB and MAF) [59]. The intensity of individual texture components may change by either the material or process variables. Another important observation is the through-thickness heterogeneity of texture in ECAP processing, which is manifested in intensity and deviation of texture components from the ideal simple shear location. It was also observed that the texture tends to saturate with increasing the number of passes. The number of passes after which the texture saturates depends on the material. Texture saturation is reported in materials with different crystal structures. In Mg exemplifying HCP structure, a clear dependence of mechanical properties on the ECAP-induced texture was reported. In other shear-based SPD processes such as HPT and FSP, the texture strength is weakened much faster. Texture heterogeneity is well manifested in the HPT- and FSP-processed materials. It should be noted that texture is significantly influenced by large strain induced in the HPT method and by the temperature rise during the FSP process. The effect of temperature rise on the texture and microstructure evolution in the HPT process was reported to be negligible [53].

Table 1- Texture components for metallic materials with FCC, BCC and HCP structures after SPD by various methods including ECAP, ARB, HPT, MDF and FSP [53]

| Crystal structure | Materail | Processing | | Texture |
|---|---|---|---|---|
| FCC | Pure Al | CAP | Route A<br>Route Bc<br>Route C | $A_1$ and C components<br>B/$\bar{B}$ components<br>$A_1$ and C components |
| | AA5109 | ECAP | Route A-3N | (Cube →$A^*_1$) or ($A^*_2$→B→$A^*_1$) depending on initial orientation |
| | AA2014 | ECAP | Route A-5N<br>Route $B_A$-5N<br>Route Bc-5N<br>Route C-5N | B/ $\bar{B}$→$A_1$→$A_2$→C<br>B/$\bar{B}$→$A_1$→$A_2$=C<br>$A_1$→B/$\bar{B}$→$\bar{A}$→$A_2$=A=C<br>A/$\bar{A}$→C→$A_2$→$A_1$→B/$\bar{B}$ |
| | AA2195 | ECAP | Route A; N≤3<br>N=4 | $A_1$,$A_2$,B/$\bar{B}$<br>$A_2$,C |
| | Pure Ni | ECAP | 1 pass<br>Route A-3N | Strongest C→$A_1$=B/$\bar{B}$<br>B/$\bar{B}$→Oblique cube →$A_2$ |
| | Ni single crystal | ECAP | 1 pass<br>Billet top<br>Billet medium<br>Billet bottom | TD-RC and C components $C_1$ and $C_2$<br>Cube |
| | Pure Cu | ECAP | 1 pass<br>Route A-3N | Strongest C→$A_1$=B/$\bar{B}$<br>$A_1$→B/$\bar{B}$ |
| | OFHC Cu | ARB | 1 pass | C,A/$\bar{A}$, B/$\bar{B}$ components |
| | Cu | ECAP | | <110>∥S1) |
| | Cu | ECAP | Route A | $A^*_1$, C strongest after N=1<br>$A^*_1$, B after N=2,3 |
| | OFHC Cu | RB | | RD rotated cube, Cube, S, Bs, Cu |
| | Pure Ag | ECAP | 1 pass<br>Route A-3N | Strongest B/$\bar{B}$ →A<br>Strongest B/$\bar{B}$ →$A_2$ |
| | Pure Al | MAC | 1 pass | {111}<110>A→{001}<110>C→{111}<112>$A^*$→{100}<001><br>Cube |
| | | | 7 pass | {001}<110>C→{111}<110>A |
| | Al-4Mg | MAC | 1 pass | {111}<112>A*→{123}<634>S→{001}<110>C→{100}<001>Cube |
| | | | 7 pass | Brass →S |
| | CP-Al | HPT | | B→C→A→$A^*$ |
| | CP-Al | HPT | | B→C→A→$A^*$ |
| | AA5086 | FSP | | C→B/$\bar{B}$ |
| | AA2024 | FSP | | $A^*_1$/$A^*_2$, and C |
| | AA2219 | FSP | | C |
| | AA7075 | FSP | | A fiber |
| | Al-Mg-Mn | FSP | | (111)[1$\bar{2}$1], (011)[100] |
| | AA5086 | ARB | < 8 pass | Cu,Bs,S, Dillamore, Cube Goss |
| | AA6016 | ARB | < 8 pass | β fiber, Cu strongest |
| | Pd-10at%Au | HPT | | B{$\bar{1}$12}<<110>/$\bar{B}${1$\bar{1}\bar{2}$}<$\bar{1}\bar{1}$0> |
| BCC | IF steel | ECAP | 1 pass | Partial <111> and {110} fibers |
| | IF steel | ECAP | Route A<br>Route $B_A$<br>Route $B_C$<br>Route C | Strong <110> fiber<br>Strong <111> fiber<br>Complete C fiber seen to pass through $D_2$-$\bar{E}$-$D_1$; strongest $D_1$ strongest<br>Nearly complete {110} and <111> fibers for all passes<br>Strongest components are:<br>F,$D_2$ for N=2<br>F,J/$\bar{J}$ for N=3<br>F, $D_1$ for N=4 |
| | IF steel | ARB | Center<br>Surface | α fiber<br>{110}<001>{110}<112> |
| | Pure Fe | ECAP | Route $B_C$ | {110} fiber ∥ED |
| | Pure V | HPT | | {110} fiber |
| | Ni50Mn29Ga21 | HPT | | Rotated cube {001}<100><br>F{110}<100> |

Table 1- Cont.

| Crystal structure | Materail | Processing | | Texture |
|---|---|---|---|---|
| HCP | Mg | ECAP | Multi-pass by route A, Bc, and C | B fiber CCW rotated about the TD axis by varying degree which is characteristic to the processing route |
| | AZ80<br>ZK60<br>WE43<br>MgLi | ECAP | Route A | <10$\bar{1}$0> fiber |
| | CP-Ti | ECAP | Route A | B fiber |
| | Mg | HPT | | B fiber |
| | Mg-Dy-Al-Zn-Zr | HPT | | P1 and B fibers |
| | CP-Ti | FSP | | Partial P fiber , P1 |
| | Zr | ARB | | Split TD basal texture |

The non-shear deformation SPD processes such as ARB and MDF also lead to a characteristic texture formation. Nonetheless, the type of texture is different in these processes. In the ARB process, initially, a texture similar to that of rolling is developed, and then the texture strengthens until getting saturated. These ARB-induced textures are stable even after annealing. On the contrary, in the MDF process, where there is a substantial change in the strain path, texture starts weakening after the first cycle. After a few MDF cycles, the texture becomes reasonably weak. Overall, there is a clear influence of strain path, material type, and microscopic phenomena associated with deformation on the texture formation in various SPD processes. Textures of SPD-processed materials are usually heterogeneous and tend to weaken after imparting large deformation, but they have a clear effect on the properties of the final product. Table 1 summarizes the texture components for metallic materials with different crystal structures after processing with different SPD methods [53].

### 4.3.5. SPD-induced microstructural modification/transformation

#### 4.3.5.1. SPD-induced diffusive and non-diffusive phase transformations

Besides grain refinement and grain growth, SPD processing may lead to both diffusive and non-diffusive phase transformations including decomposition of solid solutions, formation of supersaturated solid solutions, dissolution of precipitates in a matrix, enhanced precipitation, amorphization of crystalline phases, nanocrystallization of an amorphous matrix, redistribution and dissolution of second phases, dissolution of multiple phases in immiscible systems to form totally new structures, and possible formation of various nanostructural features such as clusters and solute segregation. It is also well known that solute elements or impurities may interact strongly with dislocations. Besides, alloying elements may also change the SFE making twinning more or less energetically favorable [60].

For example, the maximum solubility of Fe in Al increased from 0.05 wt.% to 2.2 wt. % by SPD process. SPD also produced a solid solution in the immiscible Cu-Ag eutectic system. Dissolution of cementite in SPD processed carbon steels leads to the formation of supersaturated solid solutions of C in BCC ferrite or a phase transformation from the BCC ferrite to FCC austenite [60].

The supersaturated solid solution of HPTed Al–30Zn, Al–20Zn, and Al–10Zn alloys contained about 15 wt. %, 7 wt. %, and 3 wt. % Zn, respectively, while the equilibrium solubility of Zn in Al at room temperature is below 1 wt. %. All the three supersaturated solid solutions decomposed completely after HPT, producing nano-grained Al and Zn particles simultaneously. Deformation-induced phase transformation from the BCC phase of a Co-Fe alloy to the FCC Fe and Co phases was also found which generally occurs at high temperatures above ~ 1150 K. The HPT-induced crystalline to amorphous transformation in TiNi was also reported and it was found that the deformation-induced amorphization initiated from dislocation core regions in the interior of grains and from GBs (Fig. 7). It is believed that the energy stored in the dislocations and the GBs contribute significantly to driving the crystalline to amorphous transformation [60].

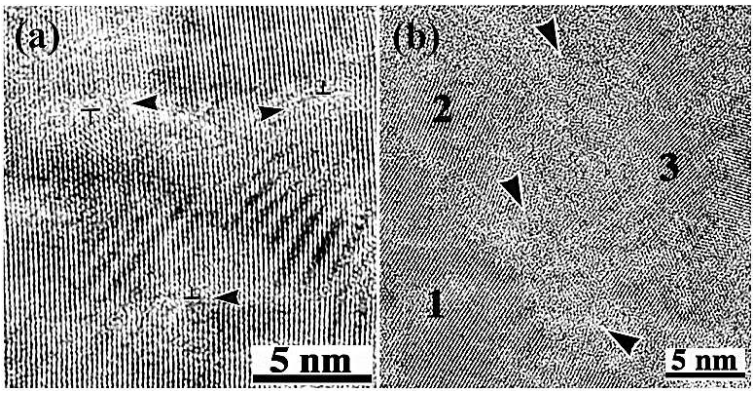


Fig. 7- (a) Amorphization initiated from dislocation cores; (b) amorphization at GBs. The numbers indicate three different grains. The arrowheads indicate the amorphous regions [60].

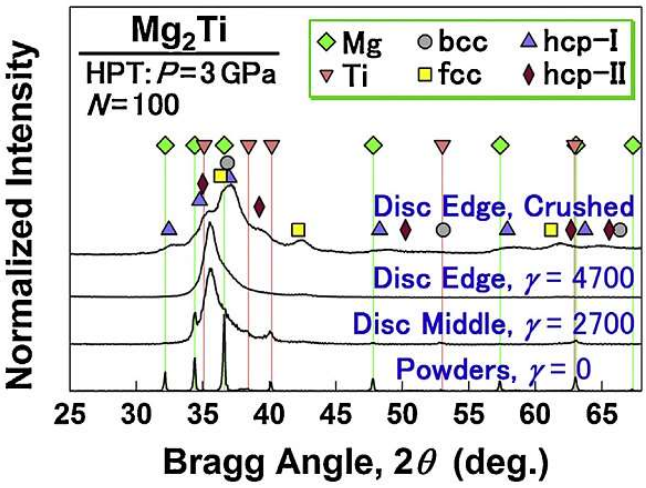


Fig. 8- XRD patterns for the Mg/Ti powder mixtures and for the middle and edge part of Mg/Ti disk samples processed by HPT [60].

Nanocrystallization of an amorphous matrix is another type of SPD-induced diffusive phase transformation. Shear banding-induced crystallization was reported in a Zr53Cu18.7Ni12Al16.3 bulk metallic glass subjected to SPD. Applying HPT on a disk of amorphous Cu60Zr30Ti10 alloy resulted in a gradient microstructure along the radial direction of the disk, with large and deformed grains in the interior of the disk and homogeneously dispersed nanocrystals embedded in the amorphous matrix at the edge part of the disk [60].

Another SPD-induced diffusive phase transformation is the dissolution and formation of totally new multiple crystal structures in immiscible systems at extremely large strains. For instance, the formation of new BCC, FCC and HCP phases in Mg-Ti and Mg-Zr systems was reported [17] by applying HPT on Mg/Ti powder mixtures for 100 revolutions and Mg/Zr powder mixtures for 100 and 1000 revolutions, although Mg is totally immiscible in Ti and Zr in both liquid and solid states (Fig. 8). Similar observations including the formation of a new BCC phase in Mg-V-based systems, a new B2 phase in Mg-Ni-Pd system, and a new amorphous phase in Mg-Ni-Sn system were reported in other immiscible systems.

Stress-induced martensitic phase transformations are common in Co, Ti, Zr, Hf, Mo, Ti alloys, and shape memory alloys. A shear-induced transformation from α-HCP to ω-simple hexagonal + β- BCC was reported in pure Zr under HPT. The pure β-Zr fabricated was stable at room temperature and atmospheric pressure. The α→ω+β transformation in Zr usually occurs under a pressure of 30 GPa, but under HPT, the required pressure was significantly reduced to 3 GPa. It is suggested that the compression together with shear forces induced by HPT result in the pressure drop needed for transformations [60].

**4.3.5.2. SPD-induced structural evolution in multi-phase alloys**

The major difference between single-phase alloys and multi-phase alloys is the existence of interphase interfaces (phase boundaries). The fundamental role of interphase interfaces is very similar to GBs, i.e., an interphase interface can act as a source, sink, and storage site of dislocations and a barrier to the motion of defects. However, they have some unique properties that GBs do not have [60]:

(1) When a dislocation line passes through a precipitate/matrix interphase interface, an Orowan loop, which is a dislocation loop surrounding the precipitate, forms and is pinned to the interface (Orowan-like strengthening effect).

(2) When a dislocation inside a low-elastic-modulus phase moves towards an interphase interface, it will experience an image force from the adjacent phase with a high elastic modulus (Koehler strengthening effect).

(3) Dislocations can be attracted to or repelled from an interphase interface by the stresses associated with the tension or compression which sustains the lattice coherency at the interface (coherency stress).

(4) Effects related to thermodynamic properties such as heat of mixing and interfacial energy. For example, as the heat of mixing decreases from a high positive value to a low negative value, the CRSS increases and then decreases.

The grain size of a multi-phase alloy is typically a few tens micrometers or even much larger. Therefore, there is plentiful space for deformation structures such as dislocation walls and deformation twins to form in the grain interiors during deformation. The high shear strain imposed by SPD can refine the grains in dual phase materials down below the UFG regime.

The phase domains can also be refined significantly and redistributed more homogeneously than in the annealed samples, as exemplified by an HPT processed Zn–22% Al eutectoid alloy shown in Fig. 9. For some dual-phase materials with outstanding plasticity such as Cu-Ag alloys, Cu-Au composites and Cu-Nb composites, the width of the phase domains can be refined down below 100 nm. Shear banding also plays an important role in the microstructural evolution of dual phase materials processed by the SPD. For example, in Fig. 10 shear banding can cause significant fragmentation of phase domains by cutting through lamellar phase bands and refine the grain structures of both phases in a localized region [60].

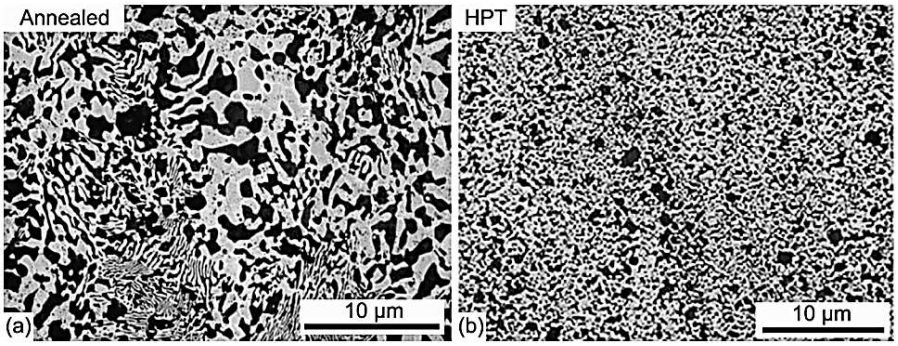


Fig. 9- Micrographs of the Zn–22% Al alloy (a) in the as-annealed condition and (b) after HPT processing for 4 revolutions [60].

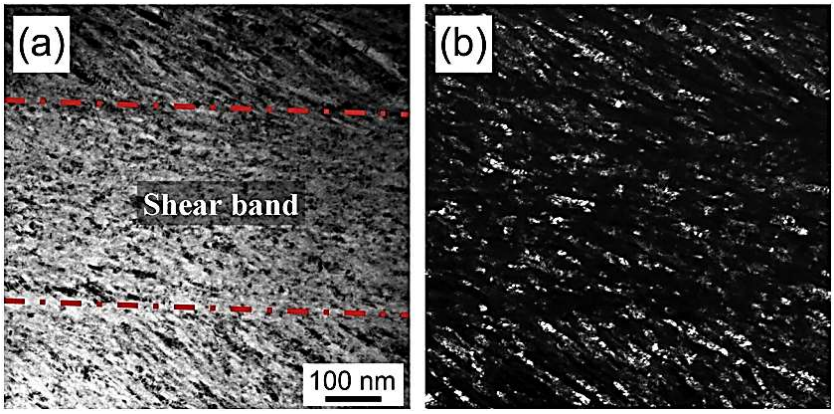


Fig. 10- (a) A bright-field TEM image and (b) the corresponding dark-field image showing a shear band structure observed in a Cu-28 wt. % Ag alloy processed by HPT for 20 revolutions [60].

Crystalline defects play a significant role in altering the precipitate morphology and matrix structures and improving the mechanical properties of the SPD processed materials. The microstructural evolution of alloys containing precipitates is significantly affected by the dislocation-precipitate interaction, GB precipitate interaction, dislocation slip, and atomic diffusion. Precipitates vary in structure, chemical stability and mechanical properties. Even for the same type of precipitates, their size, shape and density vary with the thermal processing history. All these characteristics of precipitates lead to complex microstructural evolutions of precipitates and the matrix [06].

**4.3.5.3. Evolution of precipitates during SPD processing**

Precipitates can form before, during or after SPD and the resulting microstructures can be significantly different. Some research work showed that in the course of SPD processing, pre-existing brittle precipitates with large aspect ratios can be fragmented and/or dissolved (e.g. in Al–4.11Cu, Al–1.7Cu–0.7Mg–0.3Mn) and solute atoms can be redistributed and segregated to GBs/dislocations, e.g. in AA7075 (Al-5.6Zn-2.5Mg-1.6Cu-0.4Si-0.5Fe-0.3 Mn-0.23Cr-0.2Ti) , AA6060 (Al-0.6Mg-0.6Si-0.5Cr-0.3Fe-0.1Mn-0.1Ti-0.15Zn), AA6061 (Al-1.2Mg-0.8Si-0.4Cu-0.35Cr-0.15Mn-0.7Fe-0.25Zn-0.15Ti), AA7136 (Al-9.4Zn-2.5Mg-0.12Si-0.15Fe-2.5Cu-0.2Zr-0.05Mn-0.05Cr-0.1Ti)). The fragmentation of the precipitates is exemplified in Fig. 11a, where the originally thin and flat θ′ ($Al_2Cu$) platelets in an Al alloy are bent and fragmented. The HRTEM image in Fig. 11(b) shows that the significant dislocation accumulation at the interphase interface severely distorted the coherency of the interface and caused massive cross slip to shear the large θ′ platelets into pieces [60].

The distortion of the interface can change the orientation of the precipitate and increase the interfacial energy between the precipitate and the matrix due to the change in the atomic configuration. Also, the fragmentation of precipitates reduces their aspect ratio. Subsequently, thermodynamic processes such as the dissolution of metastable precipitates and/or isotropic growth of stable/equilibrium precipitates are favored [60].

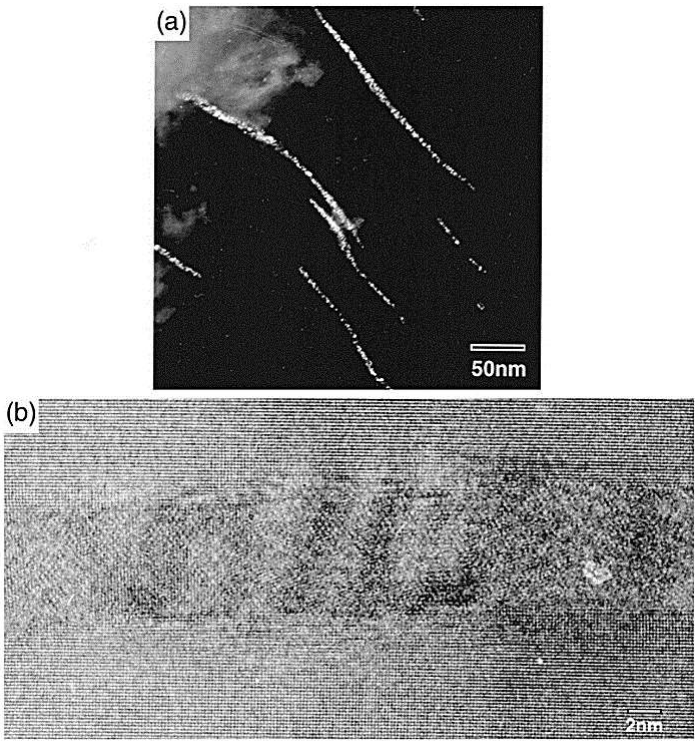


Fig. 11- (a) A dark-field TEM image taken using the (110) θ′ precipitate reflection and (b) an HRTEM image of the θ′ precipitate in the Al–1.7 at% Cu alloy after a single pass of ECAP [60].

According to the literature, there is controversy over the effects of precipitates on the rate of grain refinement in the matrix. Large (micrometer)-sized precipitates, having large interphase interfaces can block a large amount of dislocations. Accumulation of dislocations causes stress concentration at the interface. If the precipitate is non-deformable, a localized deformation zone, typically smaller than the size of the precipitate, will be created surrounding the precipitate as a result of stress gradient originated from the interface. Therefore, a sufficiently high density of large non-deformable precipitates is required to significantly accelerate the grain refinement process of the matrix phase. Moreover, nano-sized precipitates are found to promote matrix grain refinement, because of their ability to pin high density of dislocations and promoting micro-band formation. In addition, the pinning effect of nanosized precipitates on GB migration can facilitate the formation of triple junctions [60].

**4.3.6. SPD-related defects**

SPD leads to the development of high amounts of lattice defects such as vacancies, dislocations, stacking and twin faults as well as grain boundaries.

**4.3.6.1. Vacancies**

SPD-processing of metallic materials usually produces a high concentration of excess vacancies formed by non-conservative motion (e.g. climb) of dislocations during plastic deformation. These vacancies tend to form clusters for the sake of free energy reduction. SPD processing at RT yielded a very high excess vacancy concentration with the value of $10^{-4}$-$10^{-3}$ which is 17-18 orders of magnitude higher than the equilibrium vacancy concentration at RT. In thermal equilibrium, such high vacancy concentrations are only accessible at temperatures close to the melting point. Experiments on SPD processed FCC metals, such as Cu and Ni, revealed that the vacancy concentration increased monotonously with increasing the strain. The larger amount of vacancies observed for HPT-processing can be explained by the very high hydrostatic pressure in the sample which hinders the migration of vacancies to sinks [53, 61].

Deformation-induced vacancies largely diffuse to grain boundaries and the rest remains as vacancy clusters. The mean size of vacancy clusters differs, depending on the activation energy for vacancy migration in a given material: In Al and Ti, clusters are as large as 40-50 vacancies; in Fe, Ni and W, 13-14 vacancies are clustered; and Cu and Nb have clusters of merely 4 vacancies. The size distribution of vacancy clusters can be well described by the positron distribution. An example of size distribution of vacancy clusters determined by positron annihilation spectroscopy in UFG copper deformed by HPT is shown in Fig. 12 [53].

**4.3.6.2. Dislocations**

Generally, the dislocation density increases with the strain level. If the SPD is carried out at RT, the dislocations annihilation will be more difficult for a higher-melting-point material, leading to a higher dislocation density. Moreover, the lower SFE increases the splitting distance between the partials in dissociated dislocations, thereby hindering annihilation of dislocations by cross slip and climb. Increasing the solute concentration enhanced the dislocation density.

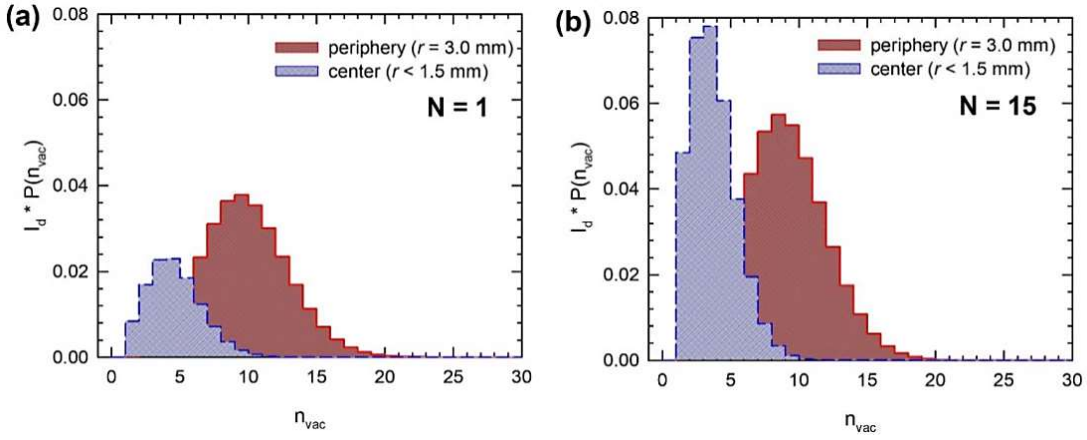


Fig. 12- Size distribution of vacancy clusters in ultrafine-grained copper deformed by HPT using (a) N = 1 revolution and (b) N = 15 revolutions, at central region (radial distance from center r < 1.5 mm) and periphery (radial distance from the center r = 3.0 mm) of disk samples. The size distribution of vacancy clusters $P(n_{vac})$ was determined by positron annihilation spectroscopy. The size distribution of vacancy clusters in the figure was multiplied by the intensity Id of positrons trapped at vacancy clusters which is a measure of the concentration of vacancy clusters [53].

The SPD method may also influence the dislocation density. As an example, Fig. 13 shows the saturation dislocation density in pure Cu obtained by different SPD methods at RT. The lowest dislocation density of ~$10\times10^{14}$ $m^{-2}$ was obtained by the MDF and TE, and the highest dislocation density of ~$40\times10^{14}$ $m^{-2}$ was achieved by HPT. [61].

This behavior of the HPT-processing is attributed to the large hydrostatic component of the applied stress field that hinders the diffusion and retards the annihilation of dislocations during HPT. In general, the difference between the dislocation densities obtained in the same material by various SPD methods can be explained by the different deformation conditions, such as the temperature, strain level, strain rate, hydrostatic pressure and degree of non-monotony of deformation. At higher SPD process temperature, the maximum achievable dislocation density is reduced. The as-processed microstructure of the material before SPD also influences the dislocation density. For instance, under the same ECAP conditions, the as-cast and as-extruded AX41 Mg alloys reached the maximum dislocation density after two and one passes, respectively [61].

It was found that the higher the melting point and the lower the stacking fault energy, the larger the saturation dislocation density in FCC metals (Fig. 14a). Increased solute concentration and secondary phase content also result in an enhanced dislocation density. Therefore, very high dislocation densities can be achieved in high-entropy alloys with low stacking fault energy [53].

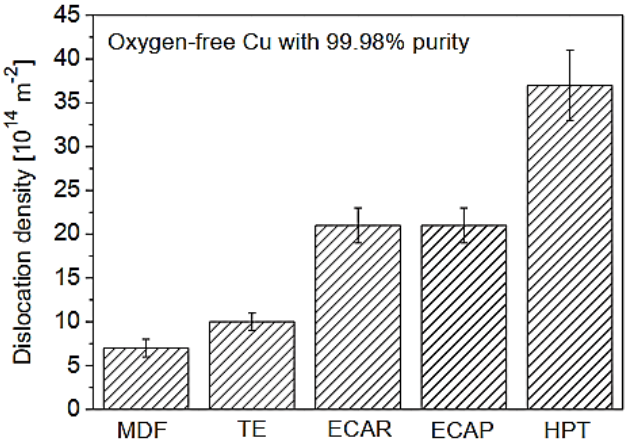


Fig. 13- The saturation dislocation density in pure Cu obtained by different SPD methods at RT [61].

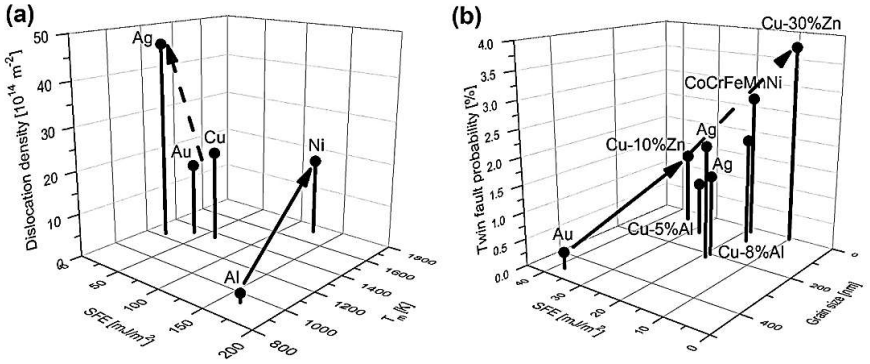


Fig. 14- (a) Maximum dislocation density as a function of melting point and stacking fault energy and (b) twin fault probability as a function of stacking fault energy and grain size for pure FCC metals processed by ECAP at room temperature. Dislocation density is higher for metals with higher melting point and lower stacking fault energy, and twin fault possibility is higher for metals with low stacking fault energy and smaller grain size [53].

#### 4.3.6.3. Stacking and twin faults

Significant amount of stacking and twin faults in SPD-processed materials with SFE< 40 mJ/m$^2$ was observed. The lower SFE is accompanied by a smaller twin fault energy which facilitates the nucleation of twins. During SPD, twin faults are usually formed at dislocation glide obstacles such as Lomer-Cottrell locks and grain boundaries. At these locations, the stress can exceed the critical value necessary for twin nucleation. In addition to lower SFE, smaller grain size also increases the likelihood of twinning in SPD-processed FCC materials. This can be explained by the increase of equilibrium splitting distance between partials of dissociated dislocations with decreasing grain size. The points in Fig. 15 represent both pure metals and alloys. It is known that alloying may reduce the SFE. For instance, the addition of 30% Zn or 16% Al to Cu decreases the SFE from ~60 to ~10 or 6 mJ/m$^2$, respectively. Therefore, alloying can result in a simultaneous reduction of grain size, increase of dislocation density and enhancement of twin fault probability [61]. The grain size also influences the occurrence of twinning (see Fig. 14b) [53].

Among the SPD techniques, the HPT results in the highest vacancy concentration, dislocation density, twin fault probability, and grain boundary area because large hydrostatic pressure applied during the process can hinder the annihilation of defects. Positron annihilation spectroscopy studies revealed that not only dislocation density increases in HPT processed materials, also vacancy concentrations as high as those at the material's melting point are approached [53].

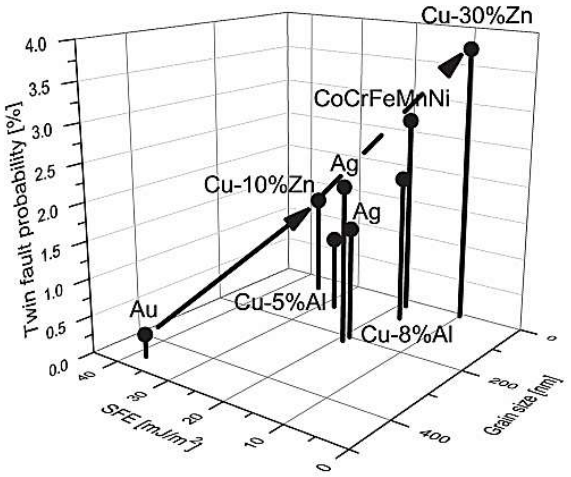


Fig. 15- The effect of SFE and grain size on the twin fault probability of UFG fcc metals and alloys processed by ECAP and HPT at RT. The solid and the dashed arrows indicate that the smaller the grain size and the SFE, respectively, the larger the saturation twin fault probability [61].

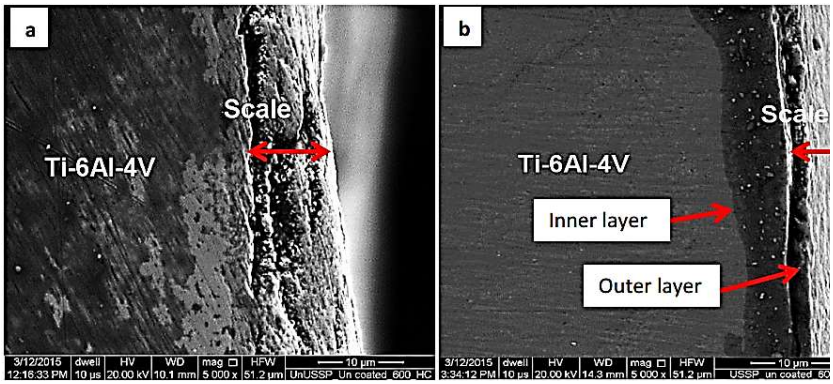


Fig. 16- Oxide scale morphology from surface towards interior across the thickness of the control samples exposed in air at 600 °C for 100h: (a) non-USSPed (b) USSPed [62].

The analysis of the homogeneity of UFG structures showed that spatial distribution of dislocations becomes uniform after a certain number of HPT revolutions. However, the lateral distribution of vacancy clusters remains non-uniform even after a high number of HPT revolutions. According to Fig. 12, the average size of vacancy clusters near the periphery is greater than that in the center of the sample. This is due to increasing strain and strain rate with increasing the radial distance from the center, which leads to an enhanced rate of vacancy production in the periphery region [53].

## 5. Hot corrosion in SPDed metals and alloys

Kumar et al. [54] investigated the effect of surface nanostructuring using ultrasonic shot peening (USSP) on the HC behavior of Ti-6Al-4V alloy in three different salt mixtures: NaCl, 75 wt.% $Na_2SO_4$ + 25 wt.% NaCl, and 90 wt.% $Na_2SO_4$ + 5 wt.% NaCl + 5 wt.% $V_2O_5$ at 400, 500 and 600 °C. Specimens were subjected to heating and cooling cycles for total exposure of 100 h.

A refined microstructure of the primary α and transformed β and micro-twins were developed in the USSPed specimen. The twins progressively subdivided the primary coarse grains into smaller ones in the HCP α-Ti, having limited slip system. The HC rate of the USSPed specimens was lower than that in the non-USSPed ones which was attributed to the grain refinement and higher density of grain boundaries [62]. The $TiO_2$ layer formed at elevated temperature (600 °C) is not fully protective causing easy inward diffusion of oxygen and its dissolution in the substrate (Fig. 16a). Corrosion products were also found to form with the formation of cavities and pits at grain boundaries, leading to easy flow of oxygen. Initially, at high temperature, a thin outer protective layer is formed on the nanostructured surface of USSPed sample which is not fully protective, but at the same time an inner protective layer is formed after breaking of this outer layer (Fig. 16b). This layer consisted of various oxide products which improved the corrosion resistance of the USSPed samples [62].

The positive effect of USSP on the HC resistance of selective laser melted (SLMed) Ti-6Al-4V alloys was studied by Srikanth et al. [63]. The samples were shot peened by hard steel balls of 3 mm diameter and vibrational amplitude of 80 μm for 3 min. It was shown that the microstructures of both non-USSP and USSP samples were martensitic phase with a noticeable difference in the flake length. The flake length in non-USSP sample was 62.4 ± 6.5 μm and it reduced to 39.3 ± 3.4 μm after the USSP. The reduction in flake length was attributed to the grain refinement. The non-USSP and USSP samples were corroded at 750°C in air, and $Na_2SO_4$ + 25 % NaCl and $Na_2SO_4$+ 50 %$V_2O_5$ salt mixtures. The maximum and minimum weight gains were observed in the sample exposed to $Na_2SO_4$+ 50 % $V_2O_5$ and air, respectively. In almost all conditions, the USSP samples showed lower weight gain than the non-USSP samples (Fig. 17). The increase in the oxidation and HC resistance in the USSP samples was described by the grain refinement which allows the formation of strong and protective $TiO_2$, $Al_2O_3$ passive film [63].

The reduced grain size or increasing in grain boundary area will create short path to the solute to diffuse, resulting in increased diffusivity of solute atoms. This will enhance the activity of oxygen towards Al to form stable $Al_2O_3$ film that protects material from further corrosion [63].

Chakkravarthy et al. [64] studied the effect of abrasive water jet peening on the NaCl-induced HC (at 600°C for 100 h) behavior of Ti–6Al–4V. The experimental setup and the optimum process parameters of the AWJ processing are shown in Fig. 18.

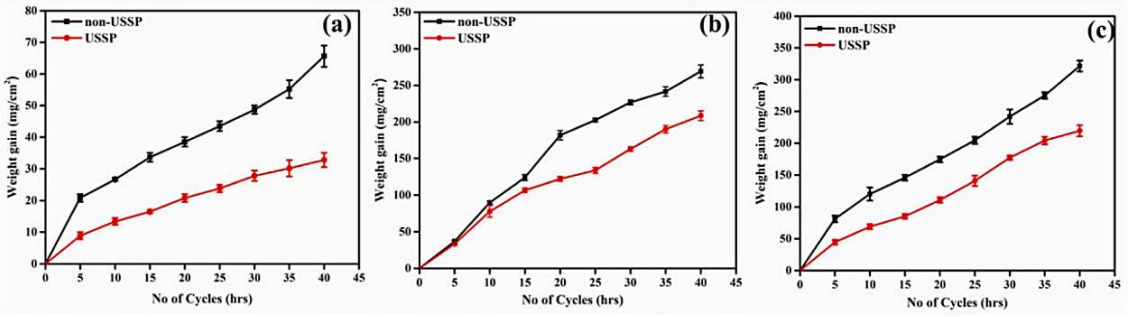


Fig. 17- Comparison of the weight gain vs. number of cycles of non-USSP and USSP samples corroded in (a) air, (b) $Na_2SO_4$ + 25 % NaCl salt, (c) $Na_2SO_4$ + 50 % $V_2O_5$ salt [63].

It was shown that the AWJ peened surface exhibited 2.5 times better corrosion resistance than that of the pristine surface (Fig. 19). Moreover, the oxide scale on the pristine surface was porous and thicker, consisting of $TiO_2$, $Al_2O_3$, $V_2O_3$, and $V_2O_5$. Based on the observations, it was determined that infiltration of chloride ions into the alloy surface initiated corrosion and also released a large volume of chloride gasses [64].

Conversely, the AWJ peened surface had a thinner and compact passive film. The lower mass gain of the AWJ peened surface could be attributed to compressive residual stresses on the surface, which retards the subsurface diffusion of chloride ions (Fig. 20). Comparing the HC resistance of AWJ peening with USSP, it was observed that the latter was relatively more effective possibly due to a larger sub-surface layer with compressive residual stresses. Nevertheless, AWJ peening has great potential in preventing HC resistance of Ti–6Al–4V alloys (Fig. 21) [64].

The effect of ultrasonic surface rolling process (USRP) on the hot salt (NaCl, 500°C) corrosion fatigue (HSCF) of TC11 Ti alloy was investigated in [57]. USRP was performed at rotating speed of 56–96 rev/min, feeding rate of 0.06–0.10 mm/rev, static pressure of 0.05–0.15 MPa, and vibration amplitude of 4–8 μm. The results revealed that USRP resulted in a "peak reduction and valley filling" finishing effect on the TC11 alloy surface, significantly reducing the roughness (Fig. 22). However, as the number of passes increased, slight circumferential damage occurred, leading to a partial recovery in roughness.

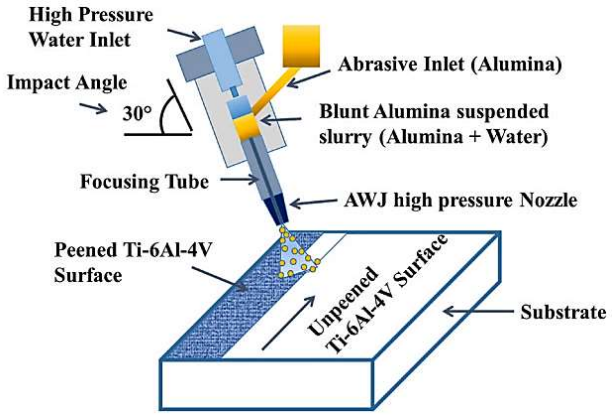


Optimal AWJ peening process parameters.

| Technical considerations for AWJ Peening process | Input |
|---|---|
| Orifice nozzle diameter [mm] | 1.9 |
| Pump pressure [MPa] | 120 |
| Impact angle [°] | 30 |
| Traverse speed [mms−1] | 7.5 |
| Stand-off distance [mm] | 40 |
| Focusing tube diameter (mm) | 0.9 |
| Abrasive mass flow rate (l/min) | 12 |
| Processing time (s/mm) | 10 |
| Abrasive material (Crushed $Al_2O_3$ balls) μm | 80 |

Fig. 18- Schematic illustration of Abrasive Water Jet peening of Ti–6Al–4V [64].

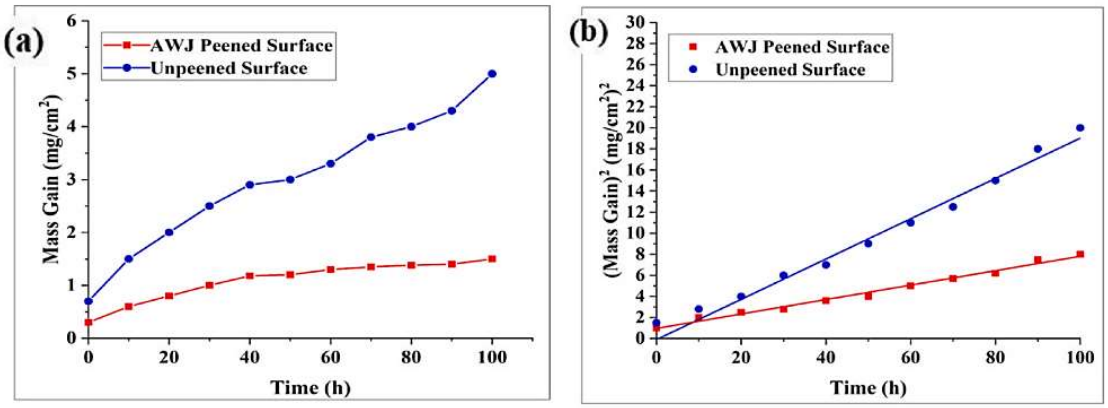


Fig. 19- Variations of (a) mass gain and (b) square of weight-gain per unit area with time of pristine and AWJ peened Ti–6Al–4V surfaces during HC [64].

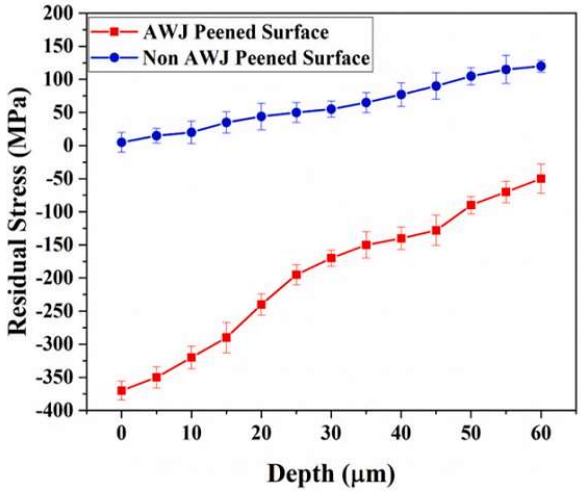


Fig. 20- X-ray residual stress analysis of pristine and AWJ peened surfaces [64].

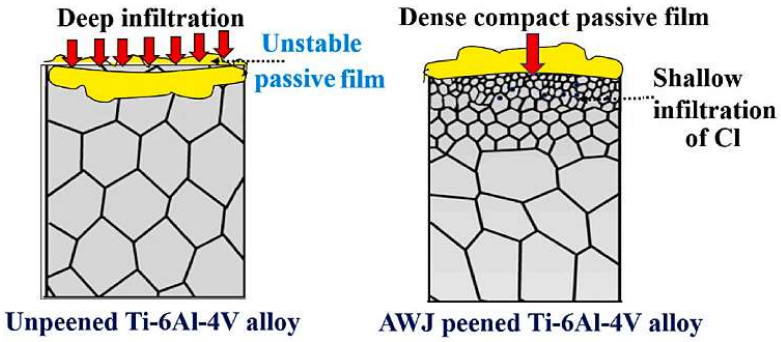


Fig. 21- Schematic illustration on passive film formation on un-peened wrought alloy and AWJ peened Ti-Al-4V surfaces [64].

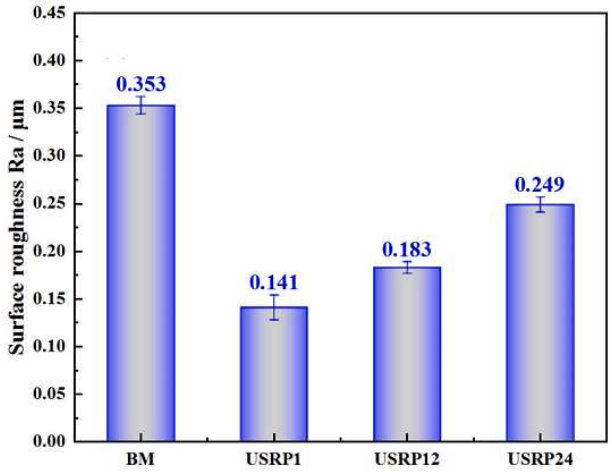


Fig. 22- Surface roughness of TC11 alloy following different passes [65].

Besides, the USRP treatment a large CRS field developed below the surface, the amount and depth of which gradually increased with USRP passes (Fig. 23) [65].

Finally, USRP significantly enhances the HSCF limit of the TC11 alloy (by 10.26%, 28.21%, and 32.05% after 1, 12, and 24 passes, respectively). This improvement is primarily attributed to the synergistic effects of the gradient nanostructure, high dislocation density, and the CRS field, which collectively inhibit crack initiation and propagation [65].

In another work of the same research team, the individual and combined effect of USRP and plasma electrolytic oxidation (PEO) was explored on the HSCF behavior of TC11 Ti alloy (NaCl, 500 °C) [66]. According to the results, the HSCF limit of the TC11 alloy increased by 10.26% after USRP treatment. This is mainly attributed to an increase of dislocation density, a decrease of β-phase content, and the introduction of a large value and deep distribution CRS field, which inhibit the occurrence of hot salt corrosion and hydrogen embrittlement of the Ti alloy, and improve the crack initiation and propagation resistance. The HSCF limit of the TC11 alloy increased by 64.10% after USRP + PEO treatment, which was significantly better than that achieved after USRP and PEO treatment alone. This is because USRP pretreatment improves the microstructure of the PEO coating, increases the thickness of drier layer, and enhances the effect of inhibiting the destructive effect of erosion elements on the substrate. In addition, the PEO coating enhances the stability of CRS introduced by USRP under thermal–mechanical coupling conditions, and synergistically improves the crack initiation and propagation resistance [66].

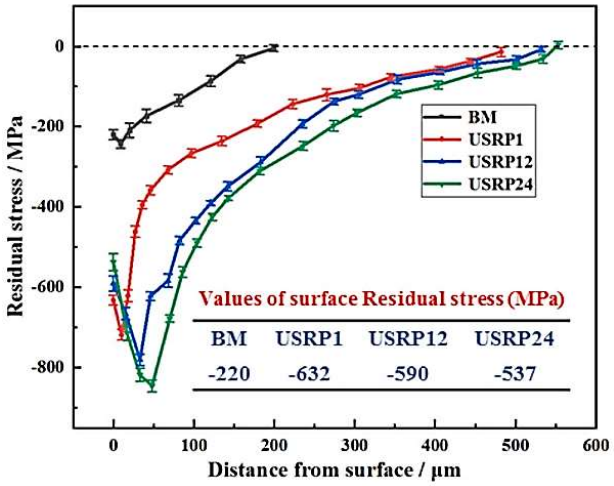


Fig. 23- Depth distributions of axial residual stress for TC11 Ti alloy before and after USRP treatment at different pass numbers [65].

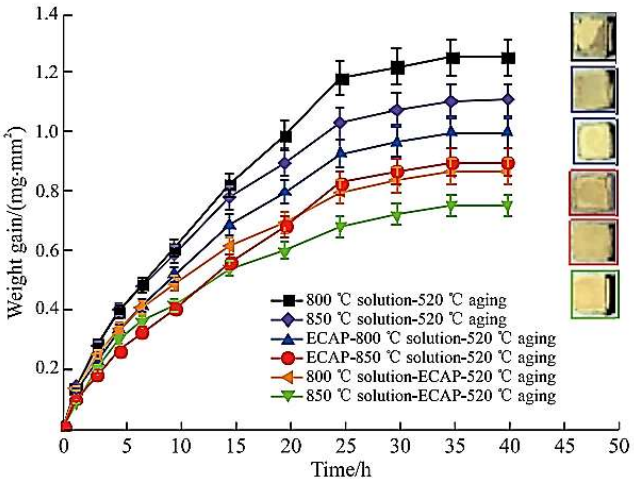


Fig. 24- Corrosion kinetics curve and macroscopic surface illustration of TB8 alloy after corrosion by secondary processing at 850 °C for 40 h [67].

In their investigation on the HC behavior of metastable β Ti alloy TB8 (Ti-12.76Mo-2.13Nb-2.73A1-0.16Si) at 850 °C for 40 h in a mixed solution of 75 wt. % NaCl-25 wt. % $Na_2SO_4$, Li et al [67] demonstrated the positive impact of ECAP (Fig. 24). This improvement was attributed to the well-refined microstructure of ECAPed sample.

The effect of low plastic burnishing (LPB) on the HC resistance of TA29 Ti alloy was studied by Kang et al. [68]. The HC tests were performed against molten NaCl salt at 600 °C for 100 h to simulate the operating temperature of hot side part such as compressor blades and discs of aircraft engines. They found that LPB processing caused grain refinement on the surface of the specimen, and formed a high density of crystal defects such as dislocations, stacking fault, grain boundaries and subgrain boundaries. That increased the diffusion channels of alloying elements, which promoted the diffusion of Al element in the matrix to the surface. The surface gradient nanostructure makes the alloying elements in the matrix diffuse more uniformly to the surface, forming a dense and continuous $Al_2O_3$ protective layer (Fig. 25). This protective layer not only effectively hinders the intrusion of O and $Cl^-$, but also inhibits the outward diffusion of Ti element in the matrix, so that the products of the inner corrosion layer is gradually converted from high valence $TiO_2$ to TiO, which attenuates the degree of internal corrosion of the LPB specimen and reduces the corrosion rate.

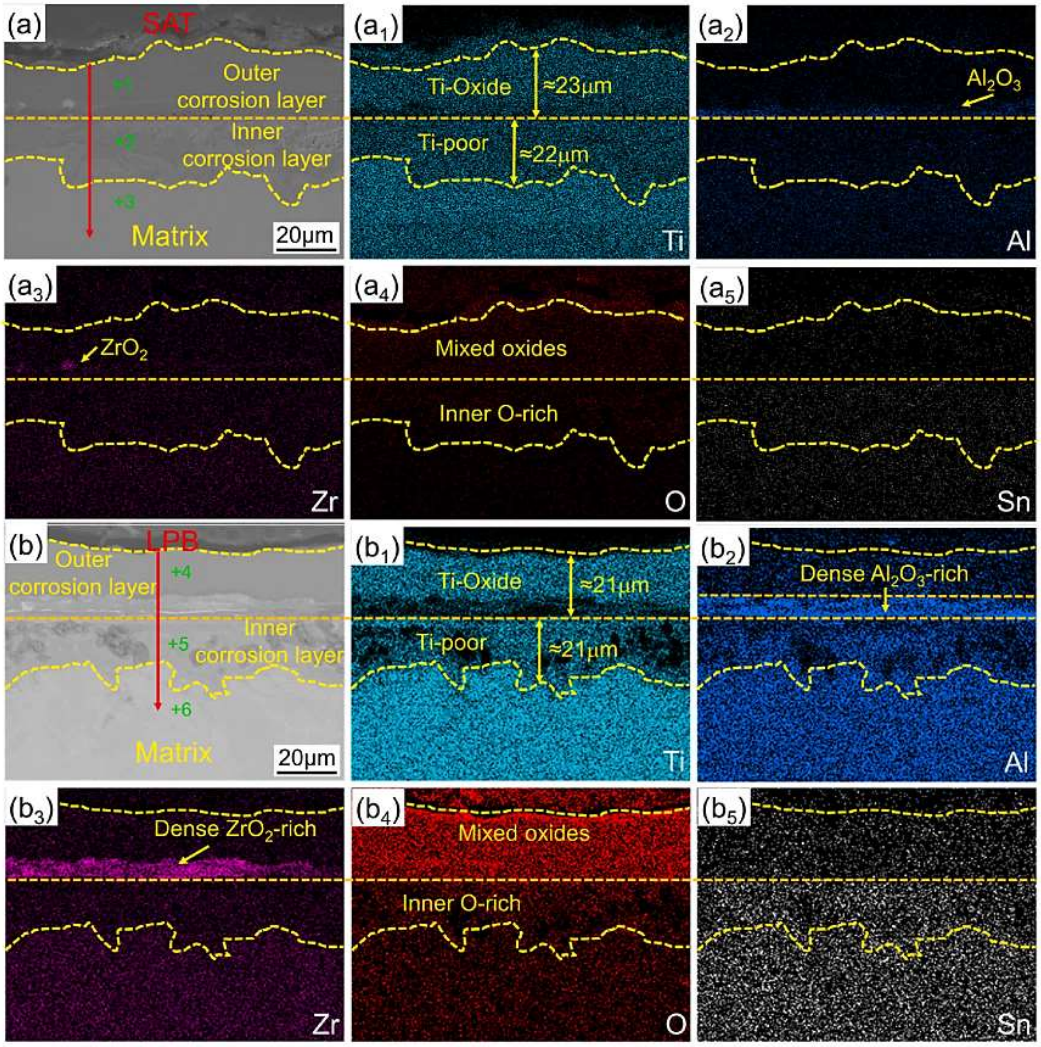


Fig. 25- The cross-section morphologies and EDS elemental mappings of the SAT (a-a5) and LPB (b-b5) after corrosion at 600°C for 100 h [68].

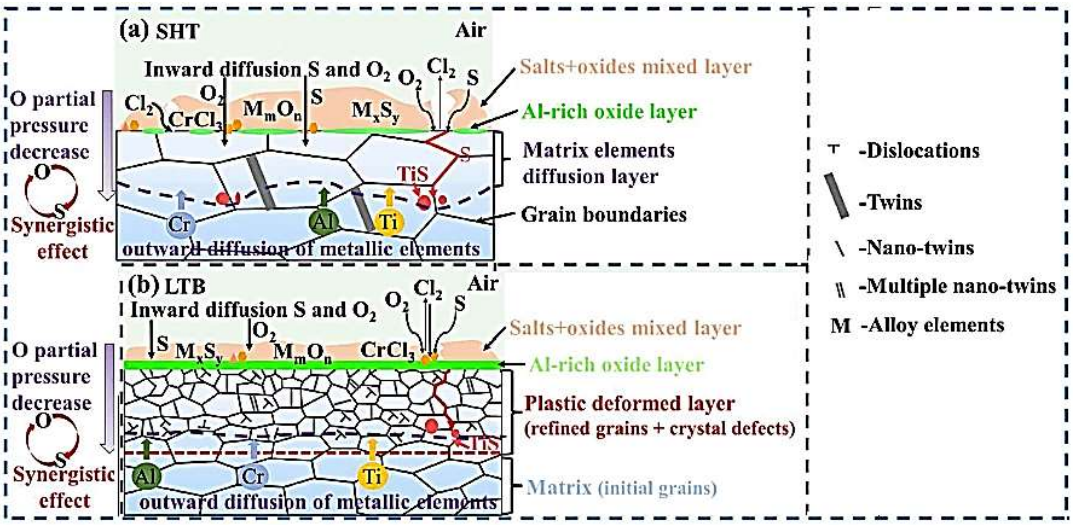


Fig. 26- Schematic diagram of the proposed HC mechanisms for (a) SHT, (b) RTM and (c) LTB treated specimens [69].

In another research work on the effect of low temperature burnishing (LTB) on the HC behavior of GH738 super alloy against molten salts (25% NaCl + 75% $Na_2SO_4$) at 700 °C for 100 h, Kang et al demonstrated that the surface grain refinement of the LTB specimens and produced numerous multiple nanotwins, which was conducive to the diffusion of Cr and Al elements from the inside to the outside of the matrix. Dense and continuous $Cr_2O_3$ and $Al_2O_3$ layers were formed on the surface of the corrosion product layer and between the external corrosion layer and the surface of the matrix, respectively, which improved the HC resistance (Fig. 26) [69].

It is inferred from the above-mentioned studies that SPD processes enhance the HC resistance of the alloys in different ways, depending on the process and alloy system. On the one hand, increasing the density of lattice defects and grain boundaries can create fast diffusion paths and accelerate protective oxides formation, as observed in USSP, ECAP, LTB, and LPB processes. On the other hand, the development of compressive residual stresses in processes like AWJP and USRP can promote the formation of a thin and compact oxide scale.

## 6. Overview and future outlook

HC causes degradation of hot section parts of gas and energy turbines, heat exchangers, concentrated solar power plants utilizing solar-salt, and etc. On this basis, numerous attempts have been made to enhance the HC performance of alloys, the most important of which are surface treatment, applying protective coatings (such as aluminide coatings, MCrAlY overlay coatings, and thermal barrier coatings) and microstructural control strategies such as grain size control and stable phase distribution that are of vital importance in the HC control.

SPD processing is also thought to be capable of improving the alloys resistance against molten salt HC. The most important reasons cited for this improvement are refinement of grains and formation of high density of crystal defects such as dislocations, stacking faults, grain boundaries, nanotwins and sub-grain boundaries which increase the diffusivity of solute atom in the surface layers and enhance the activity of oxygen towards formation of stable and protective oxide film that protects material from further HC. Development of compressive residual stresses on the surface was also reported that retards the subsurface diffusion of corrosive ions and collectively inhibits crack initiation and propagation.

However, as seen in Section 4.3.5, the microstructural consequences of SPD processing go far beyond the above. Among the notable cases are decomposition of solid solutions, generation of supersaturated solid solutions, dissolution of precipitates in a matrix, enhanced precipitation, amorphization of crystalline phases, nano-crystallization of an amorphous matrix, redistribution and dissolution of second phases, dissolution of multiple phases in immiscible systems to form totally new structures, and possible formation of various nanostructural features such as clusters and solute segregation. To the best of our knowledge, none of the previous studies have investigated the effect of one or more of the above on HC behavior of engineering alloys. This is while,

second phases may cause accelerated HC attack. Therefore, their size reduction, even distribution, and/or dissolution (formation of supersaturated solid solution) during SPD can affect the HC chemical reactions and, accordingly, the formation of protective layers and alloy response to the HC. Therefore, it is appropriate for researchers to investigate the HC performance of metals and alloys by analyzing the microstructural effects of SPD processes in more detail.

## References


1. Pettit, F., Hot Corrosion of Metals and Alloys. Oxidation of Metals, 2011. 76(1): p. 1-21.
2. Madhu, H.C., Surface Texture-Corrosion Correlation of Nickel-Based Superalloy in Aqueous and High-Temperature Conditions. Materials and Corrosion, 2025. n/a(n/a).
3. Patarini, V., N.S. Bornstein, and M.A. DeCrescente, Hot Corrosion of Gas Turbine Components. Journal of Engineering for Power, 1979. 101(1): p. 177-185.
4. Wan, X., et al., Review: hot corrosion mechanisms and corrosion resistance improvement strategies for thermal barrier coatings. Journal of Materials Science, 2025. 60(41): p. 19484-19513.
5. Wang, Q., et al., Oxidation and hot corrosion behaviors of Mo-doped NiMoAlY alloys at 750 °C. Corrosion Science, 2022. 201: p. 110262.
6. Yang, Y.Q., et al., Synergistic effect of multiple molten salts on hot corrosion behaviour of Ni-based single crystal superalloy. Corrosion Science, 2022. 204: p. 110381.
7. Chaudhuri, S. and R. Singh, High temperature boiler tube failures: case studies. Proceedings: COFA, 1997: p. 107-120.
8. Mortazavi, A., et al., High-temperature corrosion of a nickel-based alloy in a molten chloride environment – The effect of thermal and chemical purifications. Solar Energy Materials and Solar Cells, 2022. 236: p. 111542.
9. Aristu, D., et al., A comprehensive study on hot corrosion resistance of NiCoCrAlYTa and NiCrAl thermal-sprayed coatings for CSP applications. Journal of Energy Storage, 2023. 74: p. 109346.
10. Naraparaju, R., et al., Integrated testing approach using a customized micro turbine for a volcanic ash and CMAS related degradation study of thermal barrier coatings. Surface and Coatings Technology, 2018. 337: p. 198-208.
11. Nieto, A., et al., Calcia–magnesia–alumina–silicate (CMAS) attack mechanisms and roadmap towards Sandphobic thermal and environmental barrier coatings. International Materials Reviews, 2021. 66(7): p. 451-492.
12. Han, J., et al., Improving CMAS-corrosion resistance of YSZ-based thermal barrier coatings with Al2O3 addition. Surface and Coatings Technology, 2022. 446: p. 128799.
13. Wang, J.H., D.G. Li, and T.M. Shao, Electrochemical study on the hot corrosion behavior of Ni16Cr13Co4Mo alloy in molten NaCl-KCl and NaCl-KCl-Na2SO4. Corrosion Science, 2022. 200: p. 110247.
14. Iqbal, A., M.J. Khan, and G. Moskal, A review on the degradation of coatings under hot corrosion process. Contemporary problems of power engineering and environmental protection, 2022. 27.
15. Rapp, R.A., Hot corrosion of materials: a fluxing mechanism? Corrosion Science, 2002. 44(2): p. 209-221.
16. Eliaz, N., G. Shemesh, and R.M. Latanision, Hot corrosion in gas turbine components. Engineering Failure Analysis, 2002. 9(1): p. 31-43.
17. Khantisopon, K., et al., High-temperature corrosion investigations of deposit containing eutectic KCl-K2SO4 mixture on AISI 1015 and SS304 steels. Corrosion Science, 2022. 205: p. 110470.
18. de Castilho, B.C.N.M., et al., Tribology and Hot Corrosion Behavior of MCrAlY-Based Multicomponent Coatings Containing Copper. Lubricants, 2025. 13(2): p. 73.
19. Wei, B., et al., Comparing the hot corrosion of (100), (210) and (110) Ni-based superalloys exposed to the mixed salt of Na2SO4-NaCl at 750 °C: Experimental study and first-principles calculation. Corrosion Science, 2022. 195: p. 109996.
20. Cockings, H.L., et al., The effect of near-surface plastic deformation on the hot corrosion and high temperature corrosion-fatigue response of a nickel-based superalloy. Journal of Alloys and Compounds, 2020. 832: p. 154889.
21. Lu, H., et al., Effects of laser shock peening on the hot corrosion behaviour of the selective laser melted Ti6Al4V titanium alloy. Corrosion Science, 2021. 188: p. 109558.
22. Liu, R.D., et al., Preparation and hot corrosion behaviour of Pt modified AlSiY coating on a Ni-based superalloy. Corrosion Science, 2016. 104: p. 162-172.
23. Lortrakul, P., et al., Investigation of the mechanisms of Type-II hot corrosion of superalloy CMSX-4. Corrosion Science, 2014. 80: p. 408-415.
24. Varghese, A., et al., Causal discovery to understand hot corrosion. Materials and Corrosion, 2024. 75(12): p. 1639-1651.
25. Young, D.J., High Temperature Oxidation and Corrosion of Metals. 2 ed. 2015: Elsevier.
26. Lin, H., et al., Effect of AlY gradient coating on hot corrosion resistance of γ-TiAl alloy at different temperatures. Applied Surface Science, 2019. 487: p. 868-875.
27. Wu, J., et al., Effects of Ta on microstructural stability and mechanical properties of hot corrosion resistant Ni-based single crystal superalloys during long-term thermal exposure. Materials Science and Engineering: A, 2021. 806: p. 140829.
28. Gurrappa, I., Influence of alloying elements on hot corrosion of superalloys and coatings: Necessity of smart coatings for gas turbine engines. Materials Science and Technology, 2003. 19(2): p. 178-183.
29. Stringer, J., High-temperature corrosion of superalloys. Materials Science and Technology, 1987. 3(7): p. 482-493.
30. Otsuka, N. and R.A. Rapp, Hot Corrosion of Preoxidized Ni by a Thin Fused Na2 SO 4 Film at 900°C. Journal of The Electrochemical Society, 1990. 137(1): p. 46.
31. Bornstein, N.S., M.A. DeCrescente, and H.A. Roth, The relationship between relative oxide ion content of Na2SO4, the presence of liquid metal oxides and sulfidation attack. Metallurgical Transactions, 1973. 4(8): p. 1799-1810.
32. Grégoire, B., et al., Effect of chromium and silicon additions on the hot corrosion resistance of nickel aluminide coatings. Corrosion Science, 2023. 224: p. 111517.
33. Wang, X., et al., Chlorine-induced high-temperature corrosion characteristics of Ni-Cr alloy cladding layer and Ni-Cr-Mo alloy cladding layer. Corrosion Science, 2023. 216: p. 111102.
34. Ma, J., et al., Hot corrosion properties of composite coatings in the presence of NaCl at 700 and 900°C. Corrosion Science, 2013. 70: p. 29-36.
35. Yu, M., et al., Improved oxidation and hot corrosion resistance of Ta-doped NiAlY alloy at 750°C. Materials and Corrosion, 2021. 72(12): p. 1843-1853.
36. Bhuyan, P., et al., A novel approach combining grain boundary engineering and grain boundary serration to enhance high-temperature hot corrosion resistance in Alloy 617. Materialia, 2022. 23: p. 101451.
37. Mannava, V., et al., A distinct role of microstructure on hot corrosion behaviour of additively manufactured IN718. Corrosion Science, 2024. 241: p. 112550.
38. Taghiabadi, R. Ultrasonic surface severe plastic deformation of selective laser melted metal parts- A review. Journal of Ultrafine Grained and Nanostructured Materials, 2025; 58(2): p.161-196.
39. Izi, A., Honarpisheh, M., Ahmadi, F. Non-uniform simple shear extrusion (NUSSE) technique as a novel sever plastic deformation technique. Journal of Ultrafine Grained and

Nanostructured Materials, 2024; 57(1): p. 9-18.
40. Volokitin, A., Kuzmin, S. Obtaining long products by severe plastic deformation methods: A Review. Journal of Ultrafine Grained and Nanostructured Materials, 2023; 56(1): 84-98.
41. Estrin, Y. and A. Vinogradov, Extreme grain refinement by severe plastic deformation: A wealth of challenging science. Acta Materialia, 2013. 61(3): p. 782-817.
42. Azushima, A., et al., Severe plastic deformation (SPD) processes for metals. CIRP Annals, 2008. 57(2): p. 716-735.
43. Segal, V.M., et al., Fundamentals and engineering of severe plastic deformation. 2010.
44. Bagherpour, E., et al., An overview on severe plastic deformation: research status, techniques classification, microstructure evolution, and applications. The International Journal of Advanced Manufacturing Technology, 2019. 100(5): p. 1647-1694.
45. Langdon, T.G., Recent advances in using severe plastic deformation for the processing of nanomaterials. Nanoscale, 2025. 17(30): p. 17417-17427.
46. Kasaeian-Naeini, M., M. Sedighi, and R. Hashemi, Severe plastic deformation (SPD) of biodegradable magnesium alloys and composites: A review of developments and prospects. Journal of Magnesium and Alloys, 2022. 10(4): p. 938-955.
47. Naseri, M., Reihanian, M., Borhani, E. EBSD characterization of nano/ultrafine structured Al/Brass composite produced by severe plastic deformation. Journal of Ultrafine Grained and Nanostructured Materials, 2018; 51(2): p. 123-138.
48. Fatemi, M., Zarei-Hanzaki, A. Review on ultrafined/nanostructured magnesium alloys produced through severe plastic deformation: microstructures. Journal of Ultrafine Grained and Nanostructured Materials, 2015; 48(2): p. 69-83.
49. Mollaei, N., Fatemi, S. M., Abootalebi, M., Razavi, H. Zinc based bioalloys processed by severe plastic deformation – A review. Journal of Ultrafine Grained and Nanostructured Materials, 2020; 53(1): p. 39-47.
50. Aali Majidabad, M., Rezaei, A. R., Sabour, M. R., Faraji, G. Mechanical properties and pitting corrosion behavior of Al5085 alloy processed via ECAP. Journal of Ultrafine Grained and Nanostructured Materials, 2023; 56(1): p. 42-49.
51. Zhang, L. and Z. Wu, A mini-review of surface severe plastic deformation methods and their effects on steel and stainless steel. Proceedings of the Institution of Mechanical Engineers, Part L: Journal of Materials: Design and Applications, 2023. 238(3): p. 397-415.
52. Nemati, R., Taghiabadi, R., Saghafi Yazdi, M., Amini, S. Corrosion behavior of ultrasonic impact treated Haynes 25 superalloy. Journal of Ultrafine Grained and Nanostructured Materials, 2025; 58(1): p. 67-77.
53. Edalati, K., et al., Nanomaterials by severe plastic deformation: review of historical developments and recent advances. Materials Research Letters, 2022. 10(4): p. 163-256.
54. Valiev, R.Z., B. Straumal, and T.G. Langdon, Using Severe Plastic Deformation to Produce Nanostructured Materials with Superior Properties. Annual Review of Materials Research, 2022. 52(Volume 52, 2022): p. 357-382.
55. Zhu, Y.T. and T.G. Langdon, The fundamentals of nanostructured materials processed by severe plastic deformation. JOM, 2004. 56(10): p. 58-63.
56. Sato, M., et al., Formation of nanocrystalline surface layers in various metallic materials by near surface severe plastic deformation. Science and Technology of Advanced Materials, 2004. 5(1-2): p. 145.
57. Pu, P. and T. Chen Nanostructured Metals with an Excellent Synergy of Strength and Ductility: A Review. Materials, 2022. 15, 6617 DOI: 10.3390/ma15196617.
58. Faraji, G., H.S. Kim, and H.T. Kashi, Severe plastic deformation: methods, processing and properties. 2018: Elsevier.
59. Suwas, S. and S. Mondal, Texture Evolution in Severe Plastic Deformation Processes. MATERIALS TRANSACTIONS, 2019. 60(8): p. 1457-1471.
60. Cao, Y., et al., Structural evolutions of metallic materials processed by severe plastic deformation. Materials Science and Engineering: R: Reports, 2018. 133: p. 1-59.
61. Gubicza, J., Lattice Defects and Their Influence on the Mechanical Properties of Bulk Materials Processed by Severe Plastic Deformation. Materials Transactions, 2019. 60(7): p. 1230-1242.
62. Kumar, S., et al., Hot corrosion behaviour of Ti–6Al–4V modified by ultrasonic shot peening. Materials & Design, 2016. 110: p. 196-206.
63. Srikanth, M., et al., Enhancement of high temperature oxidation and hot corrosion resistance behaviors of selective laser melted Ti6Al4V by ultrasonic shot peening. Materials Chemistry and Physics, 2025. 332: p. 130170.
64. Chakkravarthy, V., et al., Effect of abrasive water jet peening on NaCl-induced hot corrosion behavior of Ti–6Al–4V. Vacuum, 2023. 210: p. 111872.
65. Zhao, W., et al., Suppressing hot salt corrosion fatigue damage in TC11 alloy at 500 °C via ultrasonic surface rolling. Surface and Coatings Technology, 2026. 522: p. 133177.
66. Shi, H., et al., Effect of the ultrasonic surface rolling process and plasma electrolytic oxidation on the hot salt corrosion fatigue behavior of TC11 alloy. International Journal of Fatigue, 2023. 168: p. 107443.
67. Li, S., et al., Hot Corrosion Resistance of TB8 Titanium Alloy after ECAP and Heat Treatment. Journal of Wuhan University of Technology-Mater. Sci. Ed., 2023. 38(6): p. 1440-1448.
68. Kang, C., et al., Effects of low plastic burnishing combined with self-oxygen diffusion on the hot corrosion behavior of the TA29 titanium alloy. Journal of Materials Research and Technology, 2025. 34: p. 1832-1849.
69. Kang, C., et al., Effect of surface treatment and synergistic effect of O and S elements on hot corrosion behavior of GH738 superalloy. Journal of Materials Research and Technology, 2023. 26: p. 462-476.